JACOBS UNIVERSITY

Jacobs University Bremen

School of Engineering and Science

Wind-driven stirring in the Arctic Ocean

On the stability of the Arctic halocline under strong wind stress

BSc Thesis in Physics

as part of the course
200322 Guided Research and BSc Thesis Physics

by

Matthias Aengenheyster

Bremen, May 9, 2014

Supervisor: Dr. Martin Losch

Second Reader: Prof. Dr. Joachim Vogt

Abstract

This study investigates the stability of the water column of the Arctic Ocean under large wind stress such as caused by a strong cyclone. It aims at determining whether sufficient turbulence is generated to disturb the halocline and mix warm thermocline waters to the surface. The study uses the MITgcm model to conduct both Large-Eddy Simulations (LES) on a 5×5 km grid with 10 m resolution and Pan-Arctic simulations with ≈ 28 km resolution. Cyclonic wind forcing of varying magnitude is applied. It is found that a mixed layer is established which deepens with increasing wind stress and with time. However, the simulations show that the turbulence is not sufficient to create a mixed layer deep enough to mix warm thermocline waters to the surface. It is also found that the cooling effect via latent heat fluxes dominates over the warming via upwelling. It is therefore concluded that the Arctic Ocean is very stable with respect to strong wind forcing.

Contents

1 Introduction

An important feature of the water column in the Artic Ocean is the strong halocline. Close to the surface there is a layer with low salinity and very low temperature (at or slightly above the freezing point) which is cooled by the low air temperatures and sea ice formation. During the summer the ice cover insulates the water from too much warming. The low salinity is caused by the inflow of fresher water from the Pacific Ocean through the Bering Strait and by fresh water influx (for example from the large Siberian rivers (Peterson et al., 2002)). The water that enters the Arctic Basin from the Atlantic Ocean has higher salinity and temperature and is denser. It is therefore overlaid by the cold and fresh water and a strong salinity (and hence density) gradient forms at the interface. This halocline is situated at significantly shallower depth than the thermocline caused by the warm Atlantic water. This configuration is usually very stable. The mixed layer is largely confined above the halocline and the heat from the Atlantic water is essentially trapped below (Rudels, Anderson, and Jones, 1996).

The ongoing global warming has particularly pronounced effects in the Arctic and has already resulted in a decrease of summer sea ice extent (Wang and Overland, 2009), a trend that is likely to continue. Therefore the possibility of little or no ice cover during the Arctic summer is very real in the coming decades. At the same time, stronger storms in the Arctic are both predicted and observed. For example, Vavrus et al. (2012) predict stronger cyclones with high confidence and at a rate even exceeding the declining trend in sea level pressure (SLP). In August 2012 the so-called "Great Cyclone of August 2012" (Simmonds and Rudeva, 2012) occured. It aroused much attention in the scientific community and has by some been associated with the record low in sea ice extent in the same year. Using a very simple geostrophic approach to calculate wind speeds from the radius of 4.2° latitude and depth of 14 hPa yields speeds of $v_w = 20\,\mathrm{m\,s^{-1}}$, while Zhang et al. (2013) find wind speeds in excess of $14\,\mathrm{m\,s^{-1}}$.

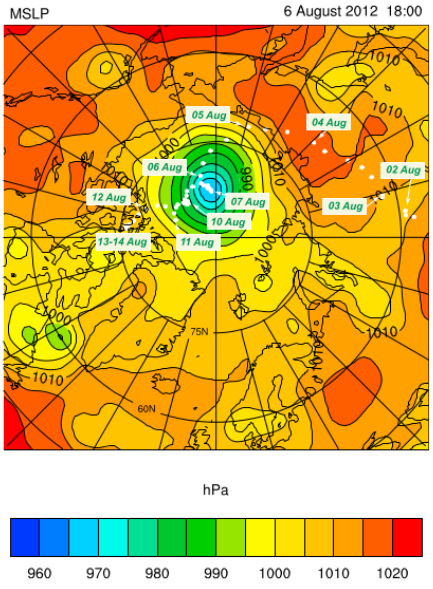

Figure 1.1: *Great Arctic Cyclone: Pressure at peak intensity (Simmonds and Rudeva, 2012)*

Confronted with the trends in both decreasing sea ice and increasing storms it is worth asking what could happen in a largely ice-free Arctic if a very strong storm (such as the "Great Arctic Cyclone" would pass the Arctic. Would it then be possible to generate enough turbulence and upwelling to disturb the halocline and mix the warm Atlantic water to the surface? If so, this could lead to a further increase in the sea surface temperature and, among other effects, enhance the decrease in sea ice or delay its formation in the

fall. This thesis attempt to answer this question. For this purpose several two- and three-dimensional simulations are conducted using the MITgcm model (Adcroft et al., 2013). The model has been selected due to its applicability to very different scales and its flexibility with regard to the problem at hand. Moreover, it contains a fully non-hydrostatic code which is an essential feature for this study.

2 Model and Physical Background

The MITgcm model is a finite-volume general circulation model (GCM) that can model both atmosphere and ocean (Adcroft et al., 2013). It supports various scales which is used in this study to investigate both large- and small-scale systems, and can be parallelized in the horizontal direction, of which frequent use has been made. Of particular importance for this study is the fully non-hydrostatic formulation (Marshall et al., 1997a) which keeps and solves all aspects of the incompressible Navier-Stokes equations since turbulent mixing is an inherently non-hydrostatic phenomenon.

2.1 Governing Equations

The momentum equations of the model for the ocean are as follows:

$$\frac{\partial \vec{v_h}}{\partial t} + (\vec{v} \cdot \nabla)_h \vec{v_h} + (2\vec{\Omega} \times \vec{v})_h + \frac{1}{\rho_c} \nabla_h p = \vec{F_h} \tag{2.1}$$

$$\frac{\partial w}{\partial t} + (\vec{v} \cdot \nabla)_z w + \hat{k} \cdot (2\vec{\Omega} \times \vec{v}) + \frac{1}{\rho_c} \frac{\partial p}{\partial z} + b = F_v \tag{2.2}$$

$$\nabla_h \cdot \vec{v_h} + \frac{\partial w}{\partial z} = 0 \quad \text{(continuity)} \tag{2.3}$$

where subscript h denotes horizontal components, z denotes vertical components, Ω is the Earth's rate of rotation, ρ_c is a reference density, $b = g/\rho_c(\rho - \rho_c)$ is the buoyancy and $\vec{F_h}$ and F_v contain forcing and dissipation terms in the horizontal and vertical directions, respectively.

The pressure is separated into surface, hydrostatic, and non-hydrostatic parts:

$$p(x, y, z) = p_s(x, y) + p_{hyd}(x, y, z) + p_{nh}(x, y, z) \tag{2.4}$$

The Boussinesq approximation is applied which neglects density fluctuations in inertial terms, and the density is split up into a reference density ρ_c and a deviation ρ':

$$\rho = \rho_c + \rho' \tag{2.5}$$

$$\rho' = \rho(\theta, S, p_0(z)) - \rho_c \tag{2.6}$$

such that ρ_c is independent of depth, while ρ' depends on depth. θ denotes potential temperature, S denotes salinity.

What follows from this are the Boussinesq equations where the density only varies in terms multiplied with the gravitational acceleration g, hence simplifying the calculations:

$$\frac{\partial \vec{v_h}}{\partial t} + (\vec{v} \cdot \nabla)\vec{v_h} + f\hat{k} \times \vec{v_h} + \frac{1}{\rho_c}\nabla_h p = \vec{F_h} \tag{2.7}$$

$$\frac{\partial w}{\partial t} + (\vec{v} \cdot \nabla)w + \frac{g\rho'}{\rho_c} + \frac{1}{\rho_c}\frac{\partial p}{\partial z} = F_v \tag{2.8}$$

$$\nabla_h \cdot \vec{v_h} + \frac{\partial w}{\partial z} = 0 \quad \text{(continuity)} \tag{2.9}$$

$$\rho' = \rho(\theta, S, p_0(z)) - \rho_c \tag{2.10}$$

$$\frac{\partial \theta}{\partial t} + (\vec{v} \cdot \nabla)\theta = Q_\theta \tag{2.11}$$

$$\frac{\partial S}{\partial t} + (\vec{v} \cdot \nabla)S = Q_S \tag{2.12}$$

where Q_θ and Q_S are forcing and dissipation terms for potential temperature and salinity, g is the gravitational acceleration, $\hat{k}$ the unit vector in the vertical, and $f = 2\Omega \sin\phi$ with latitude ϕ is the Coriolis parameter.

2.2 Boundary Conditions

At solid boundaries the condition is

$$\vec{v} \cdot \vec{n} = 0 \tag{2.13}$$

where $\vec{n}$ is a vector normal to the boundary. This applies to the bottom and the sides of the ocean, while the ocean surface is a free surface, so

$$\dot{z} = w = \frac{\partial z}{\partial t} = \frac{\partial \eta}{\partial t} \tag{2.14}$$

at $z = z_0 + \eta = \eta$, where z_0 is the position at rest (set to zero) and η the deviation caused by motion (sea surface elevation).

This study uses the no-slip condition on solid boundaries, while at the sides periodic boundary conditions are applied.

2.3 Wind Stress

The most important boundary condition at the sea surface in this model is the wind forcing. The action of the wind on the ocean is described by the wind stress $\vec{\tau}_w$ exerted on the surface. The relationship between the wind velocity and the resulting wind stress is not straightforward and depends on a large number of factors (wind speed, wind direction,

surface roughness, air pressure, waves etc.). Here always the following empirical formula will be used (Pedlosky, 1987, p. 263):

$$\vec{\tau}_w = \rho_a C_D \vec{v}_w |\vec{v}_w| \tag{2.15}$$

where ρ_a is the density of air and $\vec{v}_w$ the wind velocity. All other influences have been moved into the drag coefficient C_D. C_D can can take quite different forms. It may be assumed to be a constant or can itself depend on the wind. For instance, (Proshutinsky and Johnson, 1997) use the expression:

$$C_D = (1.1 + 0.04|\vec{v}|) \times 10^{-3} \tag{2.16}$$

2.4 Transfer of Wind Stress into the Ocean

The wind transfers momentum to the sea surface via the wind stress. The shear stress $\vec{F}_{shear}$ (one of the terms contained in the $\vec{F}$ in equations (2.7) to (2.12)) is then responsible for the downward momentum transport. It corresponds to the vertical part of the divergence of the stress tensor and can be expressed (Stewart, 2008, chap. 11.1) as

$$\vec{F}_{shear} = \frac{1}{\rho_c}\frac{\partial}{\partial z}\left(A_z \frac{\partial \vec{v}}{\partial z}\right) = \frac{\partial}{\partial z}\vec{\tau} \tag{2.17}$$

where A_z is the vertical eddy viscosity.

Integrating this over the uppermost cell in the ocean ($z \in [-\Delta z, 0]$) yields

$$\frac{1}{\Delta z}\int_{-\Delta z}^{0} \vec{F}_{shear}\, dz = \frac{1}{\rho_c \Delta z}\int_{-\Delta z}^{0} \frac{\partial}{\partial z}\left(A_z \frac{\partial \vec{v}}{\partial z}\right) dz \tag{2.18}$$

$$= \frac{1}{\rho_c \Delta z}\left[A_z \frac{\partial \vec{v}}{\partial z}\right]_{z=-\Delta z} \tag{2.19}$$

$$= \frac{1}{\rho_c \Delta z}\left(\vec{\tau}_w - A_z \frac{\partial \vec{v}}{\partial z}|_{z=-\Delta z}\right) \tag{2.20}$$

So it follows that

$$\left(A_z \frac{\partial \vec{v}}{\partial z}\right)_{z=0} = \vec{\tau}(z=0) = \vec{\tau}_w \tag{2.21}$$

So one can see the wind stress as a boundary condition of the viscosity operator at $z = 0$. Via the wind stress momentum enters the uppermost cell and then spreads vertically.

In a laminar flow the eddy viscosity A simply represents the molecular viscosity ν ($\approx 10^{-6}\,\mathrm{m^2\,s^{-1}}$ for seawater). However, the ocean is often turbulent, leading to much more effective momentum transport.

2.5 Mixing

Turbulence effectively creates motion at various different length scales. Usually the energy is put into the system at rather large scales (the wind forcing, for instance) and then transferred to smaller scales ("Energy cascade") until it is finally dissipated at a viscous scale (Adcroft et al., 2013, p. 89). This dissipation scale is called the Kolmogorov dissipation scale

$$l_k = \nu^{3/4}\epsilon^{-1/4} = (\nu^3 l_0/\tilde{v_0}^3)^{1/4} \tag{2.22}$$

where

$$\epsilon \sim \frac{v_0^3}{l_0} = \nu D^2 \tag{2.23}$$

is the fraction of the kinetic energy per unit mass that is transferred to smaller scales and finally dissipated at the viscous scale. Here l_0 and $\tilde{v_0}$ are the length and velocity fluctuation scale of the energy production scale, ν is the kinematic viscosity and D is the deformation rate at the viscous scale. At steady state ϵ is assumed to be equal for all scales between the production scale and the dissipation scale (Manneville, 2004, p. 273).

One possibility to deal with turbulence computationally is to scale the simulation such that all relevant scales down to the dissipation scale are resolved (Direct Numerical Simulation (DNS)) (Adcroft et al., 2013, p. 89). However, this scale is often very small (order of cm) so that DNS of larger systems are not feasible. Hence often, also in this work, an eddy viscosity $A \gg \nu$ is introduced which parametrizes the sub-grid-scale (sgs) momentum transport. Consequently it can be much larger than the molecular viscosity, depending on the resolved scales (Pond and Pickard, 1983).

2.6 Smagorinsky Viscosity

The code supports several parametrizations of turbulent viscosity, the standard ones being Laplacian and biharmonic viscosities. In those cases the turbulent eddy viscosity depends on the Laplacian and twice applied Laplacian of velocity, respectively.

However, these parametrizations tend to overestimate the dissipation of energy at larger scales while preferentially energy should be dissipated predominantly at very small scales (section 2.5). So Smagorinsky (1963; 1993) presented an eddy viscosity scheme in which the viscosity would be proportional to the square of the grid spacing L^2 times the horizontal deformation rate $\bar{D}$. Following the presentation of the energy cascade before, Smagorinsky assumed the energy dissipation rate to be proportional to the Smagorinsky viscosity and the square of the deformation rate $\bar{D}$ at the scale set by the viscosity:

$$\epsilon = \nu D^2 = A_{Smag}\bar{D}^2 \tag{2.24}$$

Compare equation 2.23. D is the deformation rate at the viscous scale. Using the expression for the Kolmogorov length (equation 2.22) one arrives at

$$A_{h,Smag} \propto L^2 |\bar{D}| \tag{2.25}$$

where L is the grid spacing, so

$$\begin{aligned} A_{h,Smag} &= \left(\frac{C_2}{\pi}\right)^2 L^2 |\bar{D}| \\ &= \left(\frac{C_2}{\pi}\right)^2 L^2 \sqrt{\left(\frac{\partial u}{\partial x} - \frac{\partial v}{\partial y}\right)^2 + \left(\frac{\partial u}{\partial y} + \frac{\partial v}{\partial x}\right)^2} \end{aligned} \tag{2.26}$$

Here $\left(\frac{C_2}{\pi}\right)^2$ is the proportionality constant. In the model C_2 is a variable set by the user to scale the magnitude of the Smagorinsky viscosity. In the present study it was set equal to 3.

A similar expression for the vertical Smagorinsky viscosity can be obtained via the vertical deformation rate $\bar{D}_v$:

$$\begin{aligned} A_{z,Smag} &= \left(\frac{C_2}{\pi}\right)^2 H^2 |\bar{D}_v| \\ &= \left(\frac{C_2}{\pi}\right)^2 H^2 \sqrt{\left(\frac{\partial u}{\partial z}\right)^2 + \left(\frac{\partial v}{\partial z}\right)^2} \end{aligned} \tag{2.27}$$

with the vertical grid spacing H.

Even though being a rather simple eddy viscosity scheme, the Smagorinksy viscosity is often used in LES simulations as a model for the eddy viscosity. Note however that this implementation of the Smagorinsky viscosity is still Laplacian (it depends on the square of the grid spacing). It has been proposed to introduce a biharmonic Smagorinsky viscosity which would combine the physical validity of the Smagorinsky approach with the high scale selectivity of the biharmonic operator (Griffies and Hallberg, 2000). As of now this has only been implemented in the MITgcm model for the horizontal viscosity.

2.7 Convective and Kelvin-Helmholtz Instability, Mixed Layer

There are different kinds of instabilities that can lead to turbulence and mixing. The most important ones this study are the convective and Kelvin-Helmholtz (KH) instabilities. Convective instabilities can be generated by heat flux out of the ocean. The heat loss cools the water, leading to density increase and buoyancy loss (decrease of stability).

The KH-instability, on the other hand, is caused by a velocity shear between two layers of fluid. Most clearly this occurs at the sea surface where the wind is significantly faster than the surface currents. The resulting velocity shear leads to instability and causes waves. This process occurs as well in the interior of the ocean, where it leads to internal waves and vertical mixing. An initial disturbance is exponentially amplified by concentration

of vorticity and induced vertical motion (Smyth and Moum, 2012). However, the KH-instability can only grow if the stability is below a critical value since the stratification of the water column acts against the instability. This is usually given by $\mathrm{Ri} < \mathrm{Ri}_{\mathrm{crit}} = 0.25$ (Miles, 1961) where Ri is the gradient Richardson number.

The Richardson number shows the strength of the stratification compared to the kinetic energy and is given by

$$\mathrm{Ri} = \frac{N^2}{\left(\frac{\partial|\vec{v}|}{\partial z}\right)^2} = -\frac{g}{\rho}\frac{\frac{\partial \rho}{\partial z}}{\left(\frac{\partial u}{\partial z}\right)^2 + \left(\frac{\partial v}{\partial z}\right)^2} \tag{2.28}$$

where N is the Brunt-Väisälä frequency.

The mixed layer is then the layer in which there is sufficient mixing (by turbulence) to homogenize potential temperature, salinity and potential density. It depends on the surface fluxes (heat, wind stress, fresh water) and on the stability of the water column. It is usually characterized by a rather sharp edge at the lower end, where there is steep increase in density with depth associated with a thermocline and/or halocline and a fast drop in velocity (Pond and Pickard, 1983, chap. 10.5).

2.8 Ekman Layer

For a layer close to the ocean surface the geostrophic approximation breaks down and a balance forms between Coriolis, pressures gradient and turbulent drag forces. The Navier-Stokes equations reduce to

$$(f \cdot \hat{k}) \times \vec{v} = -\frac{1}{\rho_c}\nabla p + \frac{1}{\rho_c}\frac{\partial \vec{\tau}}{\partial z} \tag{2.29}$$

with f and $\hat{k}$ as defined before. One can now split the velocity into a geostrophic part u_G balanced by the pressure gradient and an Ekman velocity u_E balanced by the turbulent stresses:

$$(f \cdot \hat{k}) \times \vec{v_E} = \frac{1}{\rho_c}\frac{\partial \vec{\tau}}{\partial z} \tag{2.30}$$

Solving this equation yields the so-called "Ekman Spiral": the current is at an angle of 45° to the right of the wind at the surface and rotates clockwise with increasing depth (on the northern hemisphere).

Then, the wind stress induces a vertical velocity

$$w_E = -\nabla \times \frac{\vec{\tau_w}}{\rho_c f} \tag{2.31}$$

At the surface $w = 0$, so $w_E = -w_G$, where w_G is the geostrophic vertical velocity. w_G is constant with depth, while w_E goes to zero at the bottom of the Ekman layer. Hence from the bottom of the Ekman layer downward w is constant (until compensated by other effects). This shows that a cyclonic wind forcing leads to a positive vertical velocity (i.e.

upwelling) in the center of the system. For the assessment of the importance of Ekman layer and upwelling the Ekman number (giving the ratio of viscous to rotational effects) and the Rossby number (giving the ratio of inertial forces to Coriolis force) are useful:

$$\mathrm{Ek} = \frac{A_h}{fL^2} \tag{2.32}$$

$$\mathrm{Ro} = \frac{U}{fL} \tag{2.33}$$

where A_h, U, and L are typical scales of eddy viscosity, horizontal velocity and length, respectively. An Ekman number close to unity and a small Rossby number correspond to equation (2.30).

3 Methods

3.1 Model Setup

3.1.1 LES

For the present study several two- and three-dimensional runs are conducted. They take place on a regular grid with $dx = dy = dz = 10\,\mathrm{m}$ with 512 cells in the x- and y-directions and 100 cells in the vertical. For the two-dimensional runs the y-extension (north) is set to 1. The setup does not include a seafloor or coastlines in order to simulate an area of open ocean far away from continental boundaries. The general setup follows the code found in the verification experiment "deep convection" and is modified as mentioned, including the three-dimensional Smagorinsky viscosity. For the advection of temperature and salt the MITgcm scheme 7 (OS7MP) is used, a seventh-order one-step method with monotonicity-preserving limiter (Daru and Tenaud, 2004). The runs in series B are run for 24 h, with the exception of run B_5 which is also run for twice that time for comparison. The two runs of series A each last 4 days.

3.1.2 Pan-Arctic Simulations

For the pan-arctic simulations an existing long term reanalysis simulation is used. It simulates (hydrostatically) the ocean-sea ice dynamics in the whole Arctic ocean and the North Atlantic down to around 50° N with a resolution of 0.25°. It uses a spherical grid rotated such that the equator passes through the North Pole and the grid cells have about equal x- and y-extension. In the vertical direction 33 levels of varying thickness are used. Vertical mixing is parametrized through the KPP mixed layer model (Large, McWilliams, and Doney, 1994). The forcing data is provided by reanalysis data from the National Center for Atmospheric Research/National Centers for Environmental Prediction (NCEP/CFSR) (Large and Yeager, 2009) while the initial data and the data at the open boundaries is taken from the "Polar science center Hydrographic Climatology" (PHC)

(Steele, Morley, and Ermold, 2001). For more details of the setup refer to Castro-Morales et al. (2014). For the purposes of the present study the setup is adapted slightly: to investigate the effects of a strong cyclone on a largely ice-free Arctic, the sea ice module is disabled (equivalent to removing all the sea ice) and the wind forcing is changed to include the artificial cyclone (while keeping the background wind forcing). The simulation is started in August 2010 and run for one month.

3.2 Initial Data

89.5 N 354.5E	80.5N 120.5E
85.5N 120.5E	82.5N 240.5E
85.5N 240.5E	88.5N 300.5E
85.5N 60.5E	85.5N 0.5E

Table 3.1: *Points used for averaging*

The potential temperature and salinity data used in this study is taken as well from the PHC, version 3.0 (Steele, Morley, and Ermold, 2001). For series A and the initial two-dimensional simulations ten points in the central Arctic are selected, the two most extreme ones discarded and the average profile obtained from the remaining ones (table 3.1). Small random fluctuations are introduced into the data (0.5 %). For the simulations of series B, an averaged profile over the Arctic Ocean is used. Here potential temperature and salinity are averaged over the region north of 70° N and between 100° to 270° E. This includes the area covered by the "Great Arctic Cyclone" at its peak intensity on August 6th, 2012 (compare figure 1.1).

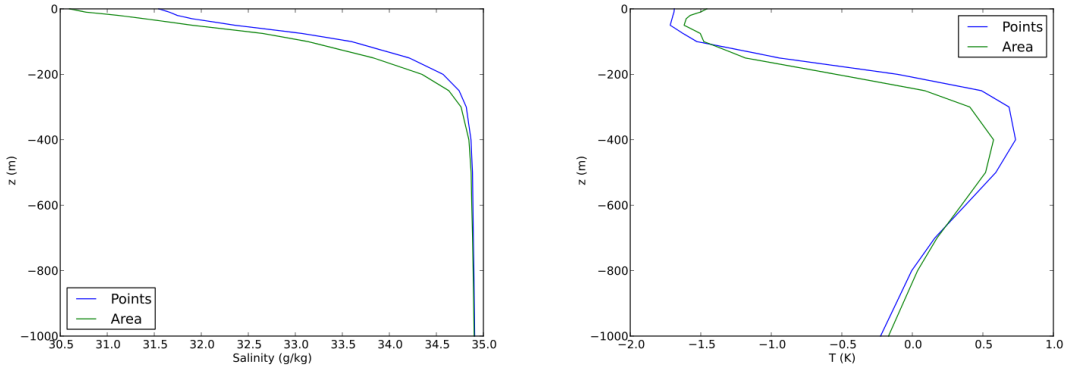

(a) *Salinity S in* $\mathrm{g\,kg^{-1}}$ **(b)** *θ in* °C

Figure 3.1: *Initial data for series A (Points) and series B (Area)*

3.3 Forcing Data

For the wind forcing several different magnitudes and patterns are used. For the two-dimensional simulations various different patterns are tested to see which ones generate larger amounts of turbulence and mixing (table 3.2).

	1st half	2nd half
1	$\tau_x = \tau_0$ $\tau_y = 0$	$\tau_x = -\tau_0$ $\tau_y = 0$
2	$\tau_x = \tau_0$	$\tau_y = \tau_0$
3	$\tau_x = \tau_0$	$\tau_y = -\tau_0$
4	$\tau_y = \tau_0$	$\tau_y = -\tau_0$
5	$\tau_x = \tau_0 \sin x$	$\tau_x = \tau_0 \sin x$
6	$\tau_y = \tau_0 \sin x$	$\tau_y = \tau_0 \sin x$
7	$\tau_x = \tau_0 \sin x$	$\tau_y = -u_0 \sin$
8	$\tau_x = \tau_0 \sin x$	$\tau_y = \tau_0 \sin$
9	$\tau_x = \tau_0 \sin x \sin \frac{4\pi t}{t_{tot}}$	$\tau_y = -\tau_0 \sin \sin \frac{4\pi t}{t_{tot}}$

Table 3.2: *Wind stress configurations for 2-dimensional runs*

In the table $\sin x$ denotes a sin wave overlaid with smaller modulation with

$$\sin x = \sin\left(\frac{2\pi x}{L/2}\right) \cdot \left(1 + 0.3 \sin\left(\frac{2\pi x}{L/12}\right)\right) \tag{3.1}$$

The three-dimensional simulations of series A use a vortex-like wind stress forcing to simulate a small low-pressure system over the area (run A_1, figure 3.2a) as well as a converging wind stress forcing (run A_2, figure 3.2b). The wind forcing in run A_1 has an average magnitude of $\langle|\vec{\tau}|\rangle = 1.33$ and in run A_2 of $\langle|\vec{\tau}|\rangle = 1.25$. The vortex itself is generated by letting both τ_x and τ_y follow a sine function with appropriate scaling (figure 3.2a). The average magnitude of the wind speed in these cases is to be of the order of Beaufort 11 ($|\vec{v}| \approxeq 30\,\mathrm{m\,s^{-1}}$) to estimate the effect of a quite strong storm. From this the wind stress is calculated using equation (2.15). In this case the drag coefficient C_D is set to the constant value of 1.2×10^{-3} for simplicity. Like in the initial data, some random noise is included to account for variations in wind and to introduce some fluctuations to start turbulence.

The wind forcing used in the later runs (series B and C) is calculated differently. Here a pressure field similar to the one shown in figure 1.1 is prescribed (essentially a gaussian function) and the geostrophic wind is calculated:

$$\rho f v = \frac{\partial p}{\partial x} \tag{3.2}$$

$$\rho f u = -\frac{\partial p}{\partial y} \tag{3.3}$$

Number	forcing factor	$\|\vec{v}\|_{max}(\mathrm{m\,s^{-1}})$	$\|\vec{\tau}\|_{max}(\mathrm{N\,m^{-2}})$
1	0.5	21.14	1.07
2	0.75	24.94	1.60
3	1	28.00	2.13
4	1.25	30.59	2.66
5	1.5	32.89	3.20
6	2.8	41.89	6.00

Table 3.3: *Wind stress configurations for Series B*

Number	forcing factor	$\|\vec{v}\|_{max}(\mathrm{m\,s^{-1}})$	$\|\vec{\tau}\|_{max}(\mathrm{N\,m^{-2}})$
1	0.5	17.79	0.66
2	0.75	21.14	1.10
3	1	28.12	2.46
4	1.25	35.32	4.73
5	1.5	42.46	8.08

Table 3.4: *Wind stress configurations for Series C*

Therefore the wind forcing for series B and C have the same form. The forcing strength is varied by introducing a forcing factor (see tables 3.3 and 3.4) that is applied to the calculated wind velocities. In series C this wind is superimposed on the wind forcing of the undisturbed simulation (using a gaussian weight function at the boundaries of the forcing region) and then directly used as forcing data. This also implies that in series C (while the location of the cyclone is fixed) the wind is only approximately constant in the region of the cyclone and not constant at all elsewhere. In series B the wind stress is calculated from the velocities using equations (2.15) and (2.16) and the model is forced with the wind stress. In these runs there is only one vortex in the domain (unlike series A) which has sufficient distance to the boundaries to mostly prevent interaction with the 'next' vortex due to the periodic boundary conditions.

For some of the two-dimensional runs and all runs of series A and B a heat forcing out of the ocean of $Q_{net} = 150\,\mathrm{W\,m^{-2}}$ is applied to account for latent heat flux due to wind (Bentamy et al., 2003) and sensible heat flux due to temperature differences. For simplicity the flux is set to a constant value over the whole domain. In series C heat forcing is provided by the NCAR/NCEP data like all other external forcings.

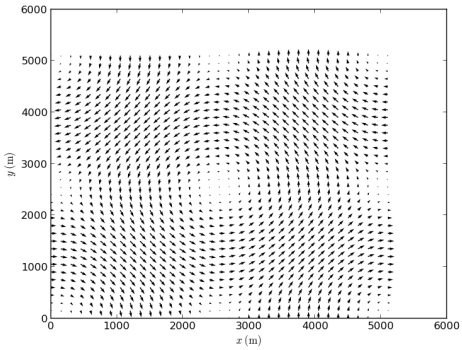

(a) *Cyclonic wind forcing for run A_1*

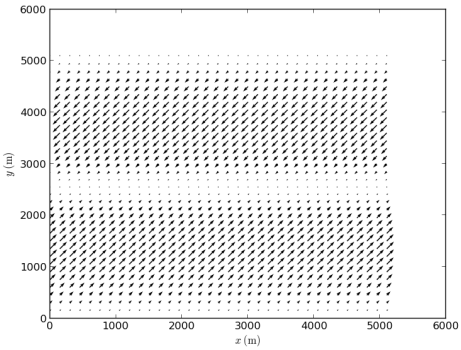

(b) *Converging wind forcing for run A_2*

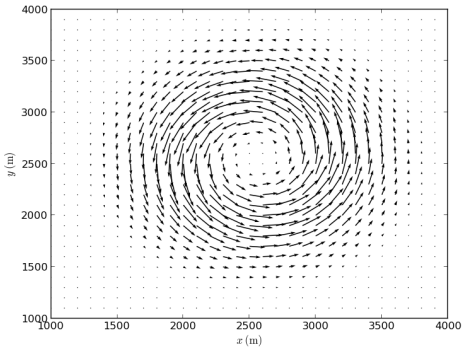

(c) *Cyclonic wind forcing of the form of series B and C*

Figure 3.2: *Wind forcings for the different series*

4 Results and Discussion

In the following section I will present and discuss the results obtained from the simulations. The important figures are included in the text, while further figures can be found in the appendix.

4.1 LES

4.1.1 2D Runs

In the runs conducted as outlined in section 3.1 it becomes clear that two-dimensional simulations, with the provided setup, are not able to generate enough turbulence for a sufficiently deep mixed layer to form. Constant wind over the whole domain generates almost no relevant dynamics while it is observed that strong spatial changes in the

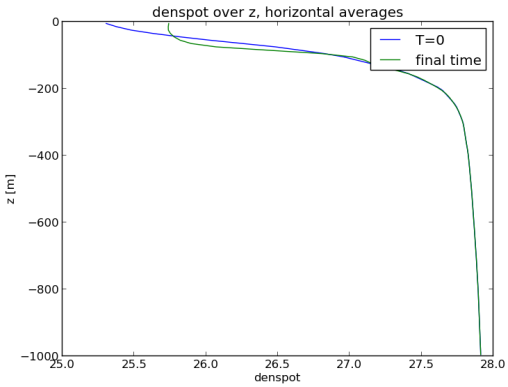

Figure 4.1: *Run 4: Potential Density over Depth, horizontally averaged, after 24 hours*

windfield (table 3.2) lead to more turbulence and mixing. After three days of simulation, mixing reaches a maximum depth of 100 m. The density profile is homogenized up to ≈ 100 m (figure 4.1), horizontal velocities decayed quickly at depths greater than 100 m (figure A.1). Note here that mixing is not equal over the domain, but turbulence, as indicated by the Smagorinsky viscosity, is strongly concentrated at the discontinuities in the surface currents (figure A.2) and continues to be confined to a small area over the whole simulation time. Downwelling (i.e. negative w) and adjacent upwelling is equally concentrated around the discontinuity. The surface current pattern which gives rise to the discontinuity is not time-independent. While mostly following the wind forcing, there are occasions of instabilities. No significant differences are observed for time-dependent forcing, and no difference is found between small random fluctuations (run 3) and spatial variation (run 7). Including heat forcing leads to lower surface temperatures and more instable surface currents, but no significant differences in the mixed layer depth.

4.1.2 Run A_1

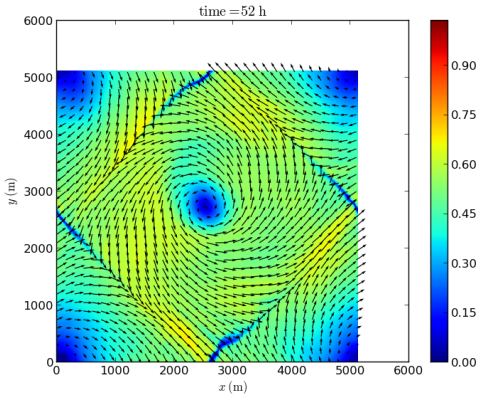

Figure 4.2: *Run A: Surface currents in* $\mathrm{m\,s^{-1}}$*, t = 52 h*

The wind forcing as shown in figure 3.2b leads to a cyclone in the center of the domain and an anticyclone in the corner. The currents generally follow the wind forcing.

The highest current speeds appear at the closest distance between the centers of the two systems (where the water masses influenced by both vortices move in the same direction), while they are lowest close to the midpoints of the sides, where counterrotating vortices move in opposite directions (figure 4.2). In these regions convergence zones form, showing very low horizontal velocities, but strongly negative vertical velocities up to $w = -0.21\,\mathrm{m\,s^{-1}}$. These regions also feature the highest Smagorinsky viscosity (indicator of turbulence) of $A_{smag} \leq 2.0\,\mathrm{m^2\,s^{-1}}$ (figure A.3).

This rhombus-structure is clearly unphysical. I believe that mainly the convergence zones are the result of the wind forcing. Firstly, the two vortices are very close to each other, in particular considering the already small domain. Hence clearly some strong

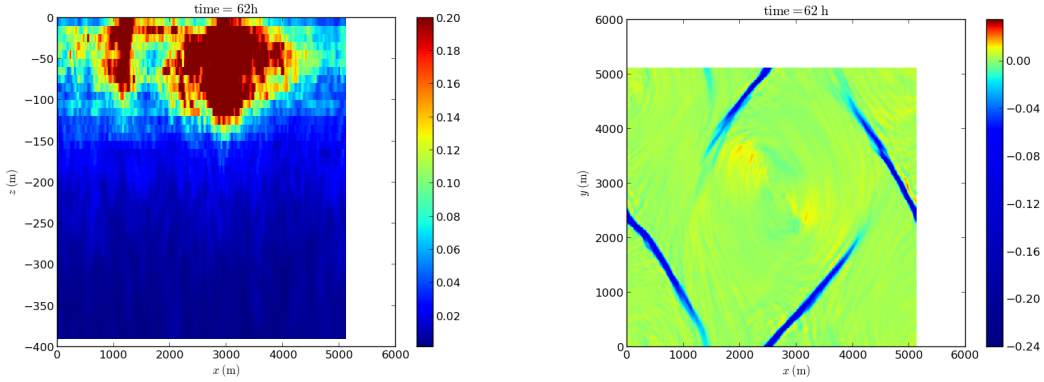

(a) $A_{h,Smag}$ *in* $\mathrm{m^2\,s^{-1}}$, $y = 500\,\mathrm{m}$ **(b)** w *in* $\mathrm{m\,s^{-1}}$

Figure 4.3: *Run* A_1, $t = 62\ h$

interaction between them is expected. Secondly, the wind forcing is not really isotropic, i.e. the forcing does not have equal strength at equal distance to the center of the vortex: at the midpoint of the line connecting the vortex centers it is strongest, while at the midpoints of the sides it is weakest. The convergence zones form around the latter points due to the low wind forcing there and the strong currents (strong wind forcing along the line connecting two midpoints) flowing towards these points from two sides. The consequence is a strong discontinuity in the surface currents, and consequently (compare section 4.1.1) strong turbulence and downwelling. In the other parts of the domain the wind forcing and hence the surface currents are much more continuous and hence form less turbulence.

A mixed layer with almost constant salinity S, potential temperature θ and potential density σ_θ is established. It is deepening with time and reaches a depth of $D_{mix} \approxeq 100\,\mathrm{m}$ after four days. The deepening slows down over time, which makes sense given that the mixing needs to work against a progressively stronger halo- and pycnocline. This is also supported by a higher-than background Smagorinsky viscosity in this depth region (and even slightly deeper) (figure 4.3a) and the fast decrease of the horizontal standard deviation of several variables below 100 m (figures A.4, A.5, A.6), indicating that the (new) halocline does not reach a depth greater than $\approx 125\,\mathrm{m}$ even after four days of strong wind. Note that the temporal change in the salinity profile is much stronger than in the temperature profile because the halocline is positioned above the thermocline and hence more affected by the turbulence.

In the center of the cyclone a temperature and salinity maximum develops over time. This suggest that upwelling should be present there since θ and S are both larger at greater depths. This is predicted by Ekman theory (equation 2.31) but hardly observed in the vertical velocity (figure 4.3b). This is probably due to the strong downwelling at the convergence zones which is one order of magnitude higher than the predicted Ekman

upwelling and probably disturbs the signal (e.g. by induced upwelling over large parts of the domain to compensated for the downwelling).

From this it is concluded that the applied strong wind forcing does lead to considerable dynamics, turbulence and the establishment of a mixed layer which deepens over time. However, the halocline is not broken and the mixed layer does not come close to the temperature maximum at $D \approx 400\,\mathrm{m}$. Furthermore, strong (and likely unphysical) convergence zones are observed which strongly enhance the mixing.

4.1.3 Run A_2

Run A_2 is a good example of a KH-instability: The surface currents quickly orient to the right of the wind stress forcing and form two counteraligned flow bands north and south of the center (figure 4.4a). The flow velocities in these bands increase until a critical threshold is reached and the pattern becomes unstable (KH instability). Then the straight band in the center with very low velocities becomes wavy and suddenly collapses, forming a counterclockwise rotating eddy (figure 4.4b). The eddy persists for a while and slowly moves around the domain before it dissolves and the two-band structure is reestablished, to be followed by yet another instability and an eddy.

Downwelling in this run (as seen by a negative vertical velocity) is mainly concentrated along leading and trailing fronts of the eddies. Since the eddy rotates counterclockwise, there is some upwelling in its center but much lower in magnitude. Therefore, θ and S show a maximum in its center. As both increase below the surface, the maxima indicate upwelling.

Also the developments in the mixed layer are quite different in this run. While in Run A_1 the Smagorinsky viscosity and the velocity in the upper layer increased with time and penetrated deeper, this is not the case here and they actually decrease from an early maximum (figure A.7). Also the increase in density and salinity in the surface layer and the penetration depth is less (figure A.8).

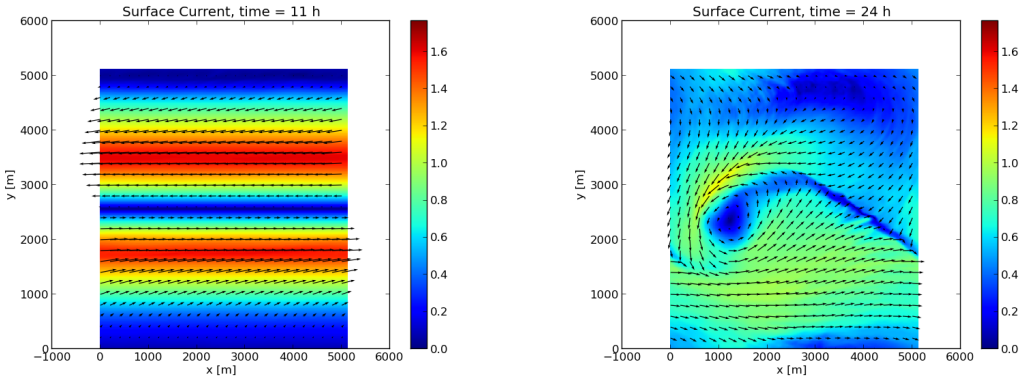

(a) *Surface currents in* $\mathrm{m\,s^{-1}}$*, t = 11 h*

(b) *Surface currents in* $\mathrm{m\,s^{-1}}$*, t = 24 h*

Figure 4.4: *Run A_2*

A possible explanation for this behavior is that the dynamics in this simulation are strongly time dependent, since they depend on the formation and dissolution of the eddies. Overall, the pattern is less constant over time. Therefore changes cannot simply penetrate deeper and deeper.

4.1.4 Series B

In this series six runs are conducted as outlined in section 3.1 with the wind forcing varied by a factor as shown in section 3.3. One explicit aim of these runs is to remove the convergence zones observed in run A_1.

One can see clearly that strong dynamics develop in the surface currents. In general the currents are cyclonic, follow the wind forcing, and are strongest in areas of largest wind forcing (figure 4.5d). However, occasionally, when the velocities have increased enough, the currents break out of the cyclonic pattern and show quite different dynamics which strongly vary with time (figure 4.5c). Then higher velocities are also observed further away from the cyclone and may persist there for some time.

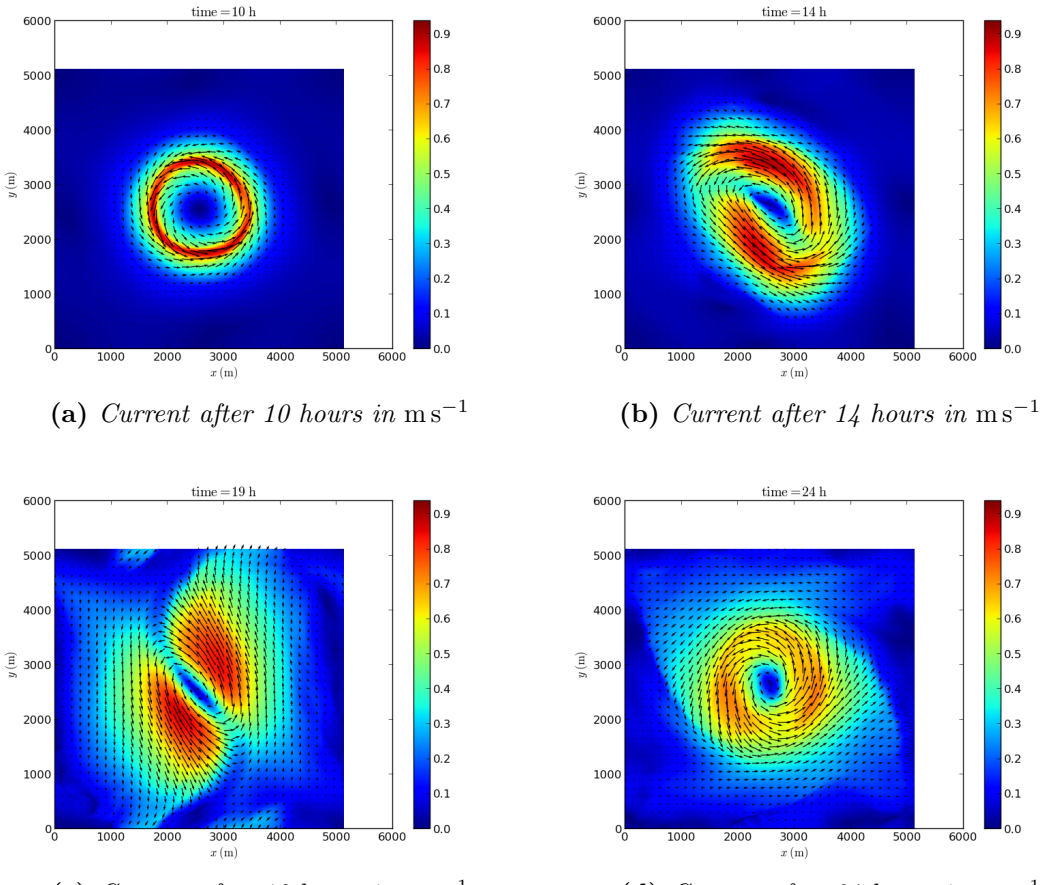

(a) *Current after 10 hours in* $\mathrm{m\,s^{-1}}$ **(b)** *Current after 14 hours in* $\mathrm{m\,s^{-1}}$

(c) *Current after 19 hours in* $\mathrm{m\,s^{-1}}$ **(d)** *Current after 24 hours in* $\mathrm{m\,s^{-1}}$

Figure 4.5: *Run B_3: Surface current development*

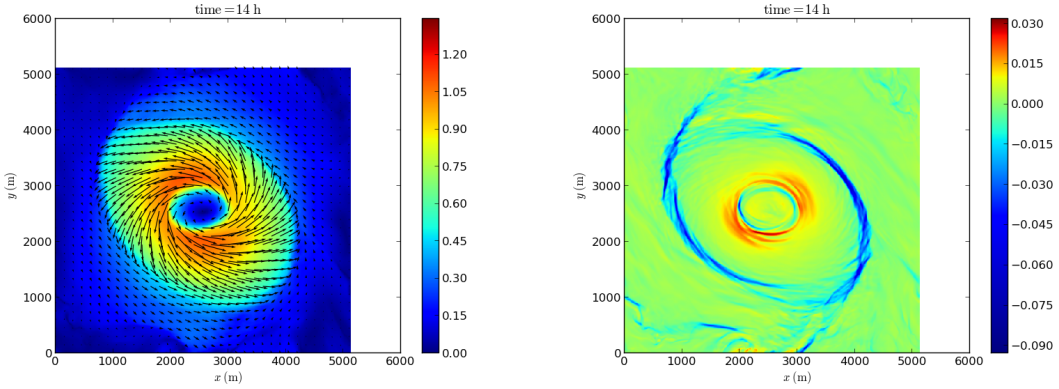

(a) *Surface current in* $\mathrm{m\,s^{-1}}$ **(b)** *Vertical velocity in* $\mathrm{m\,s^{-1}}$

Figure 4.6: *Run B_6: Surface current and vertical velocity at $t = 14$ h*

This behavior appears independent of the strength of the wind forcing and is likely an example of a KH-instability that occurs when the horizontal velocity shear becomes too large (figure 4.5a). What varies with the wind are (besides the magnitude of the velocities) the extend and timing of the fluctuations. For stronger forcing the currents break out earlier and reach further to the edge of the domain, also 'spilling' over the boundary (due to the periodic boundary conditions).

However, these 'breakouts' do not have a large effect. In particular, no such persistent convergence zones as in series A are observed in any of the runs of series B. Temporarily, zones of large vertical velocity w do develop (figure 4.6), but they do not show an unphysical rhombus structure but are rather a consequence of the temporal changes of the cyclone and its interaction with the water masses outside its influence and are hence also very time-dependent. Moreover, the magnitude of w in these regions is much weaker than in run A_1 (maximally $w \approx -0.1\,\mathrm{m\,s^{-1}}$ compared with $w < -0.21\,\mathrm{m\,s^{-1}}$ before).

Initially, as the surface currents gain in strength, there is Ekman upwelling in the center of the cyclone (figure 4.7) and downwelling along the outer edge where the fast moving water masses of the cyclone encounter water masses at much lower velocity and the velocity shear is highest (figure 4.5a).

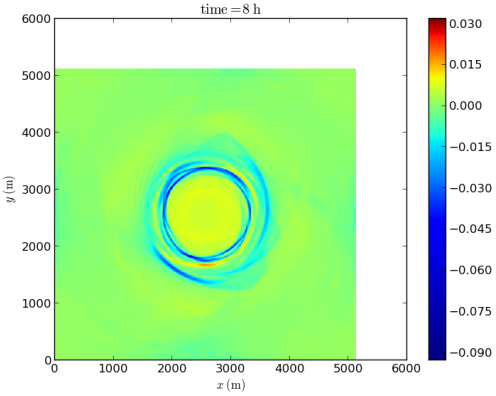

Figure 4.7: *Run B_6: w in* $\mathrm{m\,s^{-1}}$*, $t = 8$ h*

As the cyclone becomes more dynamic, upwelling continues to be mainly concentrated at the center (while also showing some downwelling there, probably due to turbulent mixing). The downwelling zones tend follow the leading and trailing 'arms' of the vortex, where a fast moving water mass collides with a much slower one (figure 4.6). These arms can be very open or almost completely encircle the cyclone. During

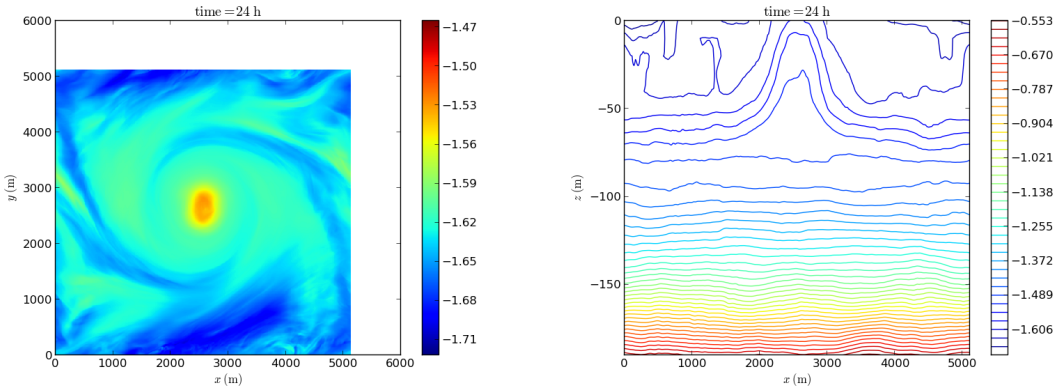

(a) θ *in* °C **(b)** θ *in* °C

Figure 4.8: *Run* B_3*:* θ *in* $x-y$ *and* $x-z$ *plane at* $t = 24$ *h*

strong outbreaks the pattern of the vertical velocity is much less clear and the upwelling in the center mostly breaks down. The magnitude of up- and downwelling increases with forcing strength ($-0.056 < w < 0.008$ for run A_1, $-0.09 < w < 0.03$ for run A_6).

From the resolution of the simulation and the observed quantities one can deduce that both the Ekman and Rossby number of the flow are large (equations 2.32, 2.33). Hence, while rotational effects are present (as shown by the upwelling in the center of the cyclone), inertial and viscous effects are more important. This is seen in the surface currents which mainly follow the wind forcing. At the beginning of the run the temperature drops very quickly in the center of the vortex from where it spreads outside, lowering the surface temperature in the whole domain. This can be explained by the vertical profile which shows a temperature minimum at very low depth ($D < 50\,\mathrm{m}$, figure 3.1b). The vortex results in upwelling via Ekman (2.31) in the center (figure A.9) and hence brings this colder water to the surface. The currents then distribute it and additionally the heat flux cools the surface. The upwelling continues which at later times leads to a temperature

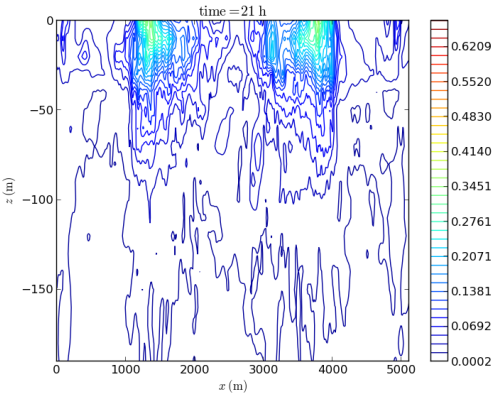

Figure 4.9: *Run* B_3*:* $A_{h,Smag}$ *in* $\mathrm{m^2\,s^{-1}}$ *at* $y = 2560\,\mathrm{m}$

maximum at the center since now warmer water masses are upwelled (figure 4.8) while the overall temperature decreases due to the heat forcing.

However, it is clearly visible that both this upwelling and the turbulence-induced mixing (figure 4.9) which primarily acts in the zones of strong wind are unable to change the temperature profile up to a depth greater than 100 m (figure A.10). Mostly these changes are even restricted to layers above 50 m (figure 4.9). The salinity behaves in a similar way although showing more variation. This, again, is due to the position of the halocline above the thermocline. The average salinity at the surface increases over time due to the mixing (which reduces the salinity at depths around 50 m). However, there is virtually no change below 100 m even for very strong wind forcing (run B_6) (figure A.11). Longer simulation times here have very a similar effect as stronger wind, however, equally the effect is too small. Using the MITgcm diagnostics package, the mixed layer depth can directly be diagnosed by the model. It returns the depth level up to which $\sigma_\theta(z) \geq \sigma_{\theta,surf} + \Delta\sigma_\theta$, where σ_θ is the potential temperature (Kara, Rochford, and Hurlburt, 2000). Figure 4.11c shows the resulting plot for run B_5.

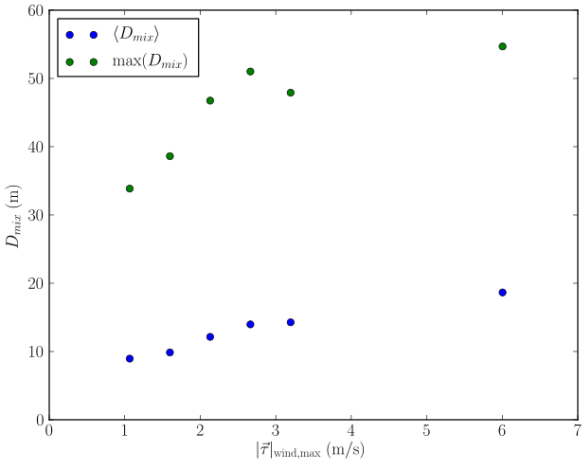

Figure 4.10: *Runs B: D_{mix} in* m *at t= 24 h*

One can clearly see that both average and maximal mixed layer depth D_{mix} increase with wind forcing (figure 4.10. However, they do so rather slowly. A factor of 6 in the wind forcing (which depends quadratically on the wind speed) causes an average deepening by only a factor of 2.

It is important to note that the average mixed layer likely underestimates it, since it averages over the whole domain of which large areas are not (strongly) affected by the cyclone. However, the tendency is clear and even the maximal mixed layer depth only increases slowly.

Therefore, it is found that the applied wind forcing is not able to generate a sufficiently deep mixed layer. This conclusion can be drawn even when the simulations lasted only for 24 h since the extension of run B_5 for another 24 h shows that the effect is similar to an increased wind forcing like in run B_6. Also, the development of the mixed layer should slow down with time (compare runs A). The computational resources did not allow a continuation of all runs B for such a long time but the conclusion is unaffected by this.

The depth of the mixed layer itself closely follows the currents. It is particularly large in areas of strong convergent currents (figure 4.11). This result is confirmed by

the slices through the center of the domain (figure 4.12) that clearly show the vortex. For the upper $\approx$ 50 m the strong uplifting of the isopycnals is obvious. The same effect can be seen for the temperature and salinity. The mixed layer depth is usually maximal at the outside of the vortex, where the turbulence ($A_{h,Smag}$) is highest.

In these regions one observes isopycnals perpendicular to the surface until a depth $D \approx 50$ m (figure 4.12). Note that the *influence* of the cyclone reaches deeper (up to $\approx$ 60 to 100 m) than the mixed layer through the Ekman-induced upwelling in the center (uplifting of isolines). However, the center of the cyclone is not diagnosed as a deep mixed layer since the density at the surface is still quite different from the one at greater depth and the isopycnals are compressed near the surface. The limit of the influence of the cyclone can be seen from the standard deviation of the salinity (figure A.12) which shows a clear cut at $D \approx 100$ m. This point also deepens with time as expected, and a similar behavior can be observed for $A_{h,Smag}$, σ_θ and the horizontal velocities.

From the plots of horizontal averages one can as well observe the ongoing mixing through the homogenization of the θ- and S-profiles and the increase in A_{smag} over time. The strong effect of the wind forcing on the observed turbulence can also be seen (compare figure A.13).

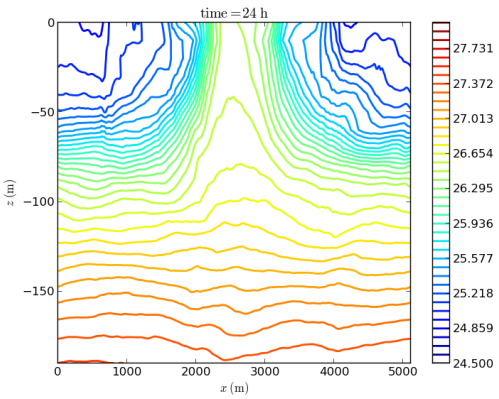

Figure 4.12: *Run B_6: σ_θ in* kg m^{-3}

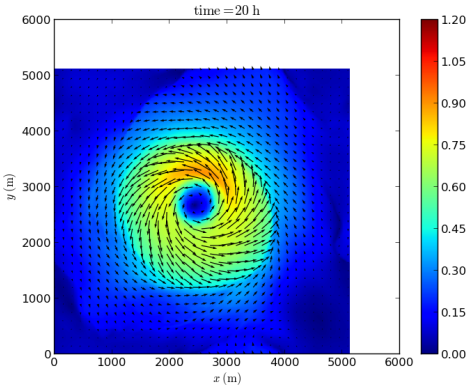

(a) *current in* m s^{-1}

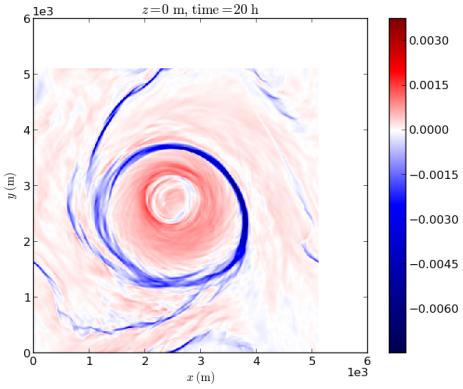

(b) $\nabla \cdot \vec{v}$ *in* m s^{-2}

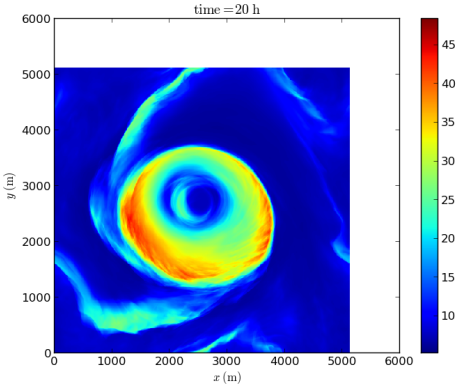

(c) D_{mix} m

Figure 4.11: *Run B_5: $t = 20$ h*

In order to investigate which factors are responsible for a deeper or shallower mixed layer, I made several attempts to find correlations between D_{mix} and other quantities (such as the current speed $|\vec{v}|$, the divergence $\nabla \cdot \vec{v}$, the wind stress itself or the Smagorinsky viscosity $A_{h,Smag}$). However, the results are inconclusive. For instance, Figure 4.13a shows the correlation between $A_{h,Smag}$ and D_{mix} and while some positive correlation seems to exist (and also seems plausible), the correlation coefficient of $R^2 = 0.46$ is rather small. Figure 4.13b shows a similar plot, but only taking points with positive wind stress curl (i.e. rather close to the center of the cyclone) and additionally colorcoding the divergence of the surface current. Again, there appears to be a positive correlation and additionally larger values of $\nabla \cdot \vec{v}$ seem to correspond to larger D_{mix} but this is also not a very clear result from a very limited region of the domain. Another sensible, but weak correlation seems to exist between $\nabla \cdot \vec{v}$ and $A_{h,Smag}$ (figure 4.13c) which suggests that convergence leads to stronger turbulence. However, all of the mentioned examples are not very solid. This could be due to the complexity of the model and/or nonlinear relationships between the quantities.

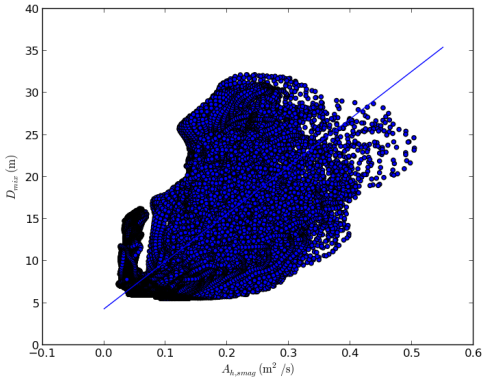

(a) *Run B_3: D_{mix} vs $A_{h,Smag}$, line gives the linear regression*

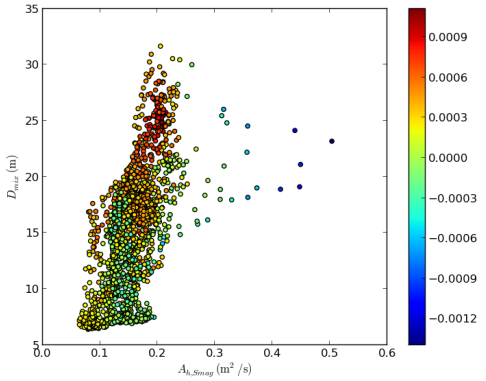

(b) *Run B_3: D_{mix} vs $A_{h,Smag}$, $\nabla \cdot \vec{v}$ is colorcoded*

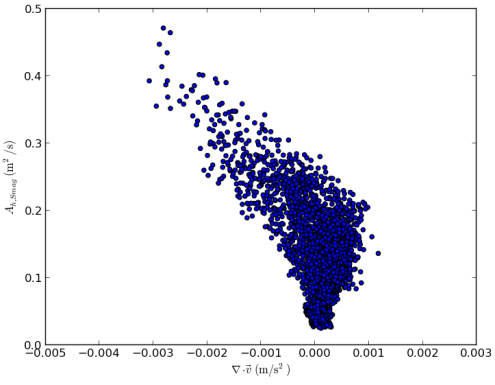

(c) *Run B_3: $A_{h,Smag}$ vs $\nabla \cdot \vec{v}$*

Figure 4.13: *Horizontal average of θ in* °C

4.2 Pan-Arctic Simulations (Series C)

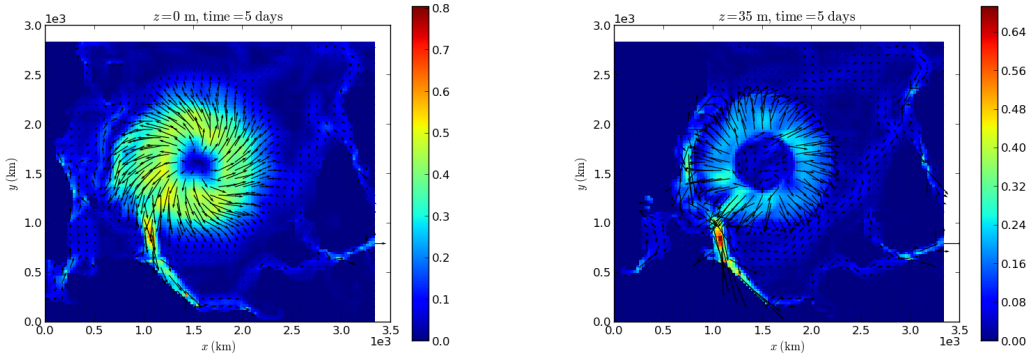

(a) *Current in* $\mathrm{m\,s^{-1}}$ **(b)** *Current in* $\mathrm{m\,s^{-1}}$

Figure 4.14: *Run C_3: Current at $z = 0\,\mathrm{m}$ and $z = 35\,\mathrm{m}$*

The currents in series C initially orient at an angle of $\approx 45°$ to the wind, towards later times they tend to align with the wind, at least in the outer regions of the cyclone. In the interior the currents stay at around 45°. The reason for this effect is the Ekman transport which, as described in section 2.8, causes surface currents to flow at angle for 45° to the right of the wind. This is confirmed by the currents at $z < 0$ which turn to the right with depth ("Ekman spiral") as expected (figure 4.14).

One can see that series C is, in contrast to series B, much more dominated by rotation. This expresses itself in an Ekman number of about unity (the basis for the Ekman balance to hold) and a small Rossby number (of ≈ 0.25), showing that the Coriolis force is much larger than inertial effects. Hence the currents follow more the direction predicted by the Ekman transport (a rotational effect important at large to planetary scales) than aligning to the wind forcing as they did in series B.

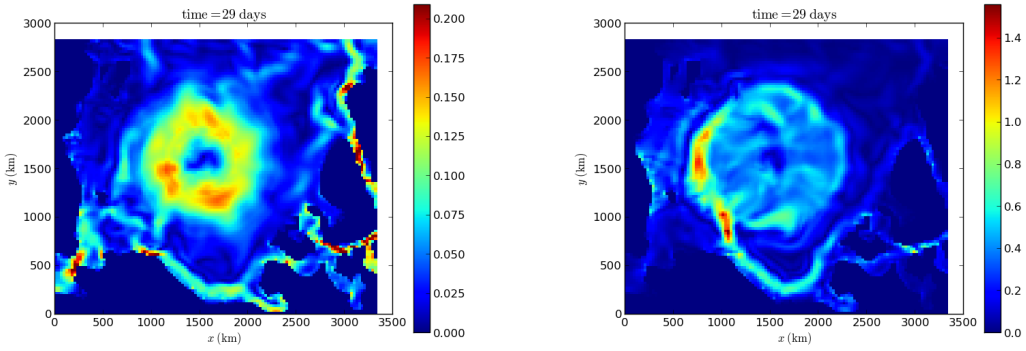

(a) *Run C_1* **(b)** *Run C_5*

Figure 4.15: *Current speed in* $\mathrm{m\,s^{-1}}$*, t = 29 days*

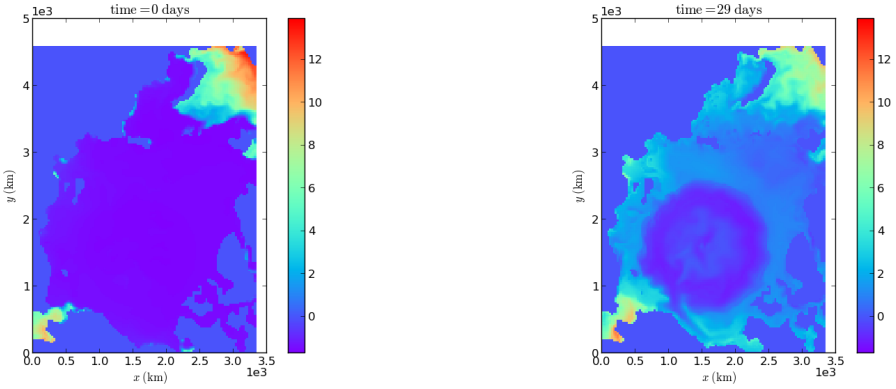

(a) *θ in* °C*, t = 0 days* **(b)** *θ in* °C*, t = 29 days*

Figure 4.16: *Run C_3: Sea surface temperature*

For weak wind forcings (run C_1) the current speed is maximal in regions of highest wind forcing (figure 4.15a) while for strong forcings (run C_5) the currents are much more influenced by topography. In particular, the current maxima are positioned at the shelf edge of the Arctic Basin. Instead of entering the shallower shelf sea, they build up flowing parallel to it, creating a strong current that flows counterclockwise along the edge of the basin (figure 4.15b). This current reaches much deeper than the surface currents in other regions and reaches still velocities $|v| > 1.5\,\mathrm{m\,s^{-1}}$ at $z = -100\,\mathrm{m}$. It appears in all runs (again, note the highly unrealistic scenario of persistent strong wind forcing) but strongly increases with forcing. It clearly heavily influences the dynamics in this run, through the transport of momentum and tracers both to deeper levels and to other regions of the basin. Hence the results are to be taken carefully. In general, one can note as well that the magnitude of the diverging current decreases over the simulation time. The most probable reason for this is the strong sea surface depression that develops under the cyclone (figure 4.17) such that the pressure gradient force starts balancing the Ekman force. This is likely also the reason for the alignment of the currents with the wind at the outskirts of the cyclone.

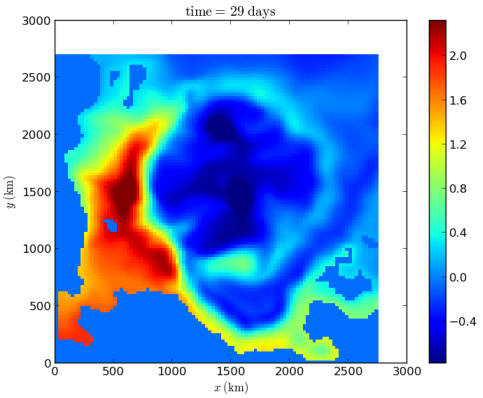

Figure 4.17: *Run C_5: Surface height anomaly η in* m

Due to the removal of the sea ice, the ocean surface is strongly warmed during the runs. Since a temperature increase reduces the density, this warming tends to increase the stability of the water column. Hence it acts against the wind-driven mixing. The area under the influence of the cyclone stays relatively cool, though not as cold as initially. It stays colder where the mixed layer is

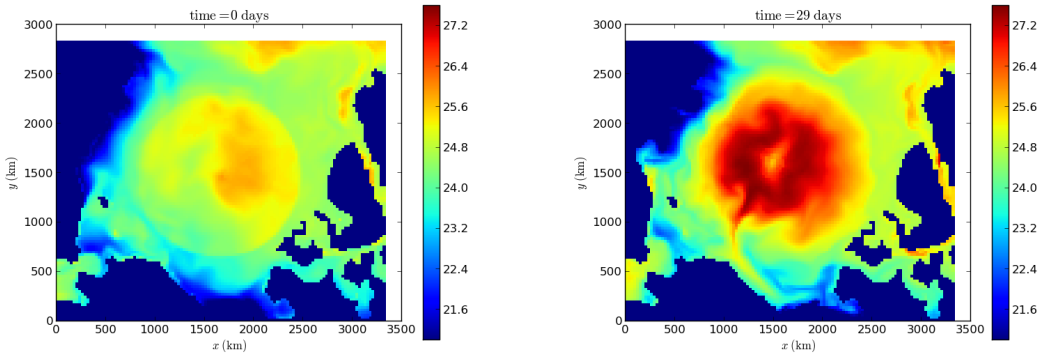

(a) σ_θ *in* $\mathrm{kg\,m^{-3}}$, t = *0 days* **(b)** σ_θ *in* $\mathrm{kg\,m^{-3}}$, t = *29 days*

Figure 4.18: *Run C_3: Sea surface density*

deeper, since here the mixing can distribute the heat more effectively. In the center of the cyclone, where winds are weaker, the temperatures are higher (figure 4.16).

The ocean under the cyclone also strongly increases in salinity. This is mainly due to upwelling and mixing which brings more saline waters to the surface. Therefore, the density at the surface increases significantly (figure 4.18), strongly decreasing the vertical density gradient and hence stability. This salinity mixing probably plays an important role in the establishment of such a deep mixed layer. The density increases to a significantly higher value than in series B ($\sigma_{\theta,max} \approx 27.3\,\mathrm{kg\,m^{-3}}$ in contrast to $26.1\,\mathrm{kg\,m^{-3}}$).

The vertical profile of the relevant quantities shows strong mixing and upwelling. At $(x, y) = (54, 41)$, a point located in the outer areas of the cyclone with strong wind forcing, the profiles of temperature and salinity are almost completely homogenized over the upper 1000 m for the strongest wind forcing (run C_5). Even the thermocline is almost removed due to the very strong Ekman upwelling (the temperature maximum is shifted upwards by more than 200 m) and the potential density is almost constant (figure A.14). However, note that S, θ, and σ_θ all show a 'step', i.e. a strong gradient, at a very shallow depth ($< 100\,\mathrm{m}$). This step in the profile is interpreted as an effect of the KPP mixed layer model: due to the large scale of the simulation it can be safely assumed that no turbulence is explicitly resolved. KPP parametrizes mixing in some boundary layer with depth h. Hence the layer above the step is homogenized by mixing, while below only Ekman upwelling is takes place, and KPP suddenly starts acting at the boundary.

In series B it was found that while mixing started from the surface and Ekman upwelling was present, no sharp step was formed (parameterizing turbulence in the same way is not possible due to the very different size). However, the mixed layer is much thinner in series B than in series C, hence KPP here appears to be a more effective method than the Smagorinsky viscosity to cause vertical mixing.

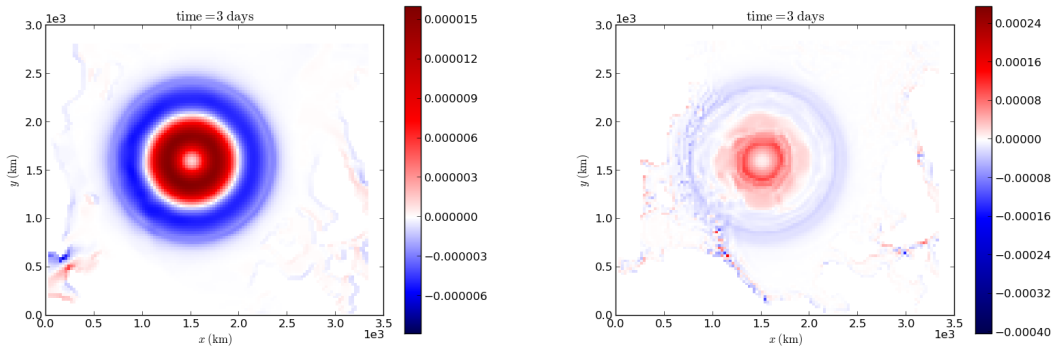

(a) $\nabla \times \tau_w$ **(b)** w $(\mathrm{m\,s^{-1}})$

Figure 4.19: *Run C_3: Wind stress curl and vertical velocity, t = 3 days*

The wind forcing in this runs has two main effects: 1) It causes strong Ekman upwelling which is proportional to the curl of the wind stress (equation 2.30, figure 4.19a). Hence we expect a positive vertical velocity at around $y = 1300\,\mathrm{km}$ and $y = 1700\,\mathrm{km}$ (where $x = 1500\,\mathrm{km}$, i.e. along the line $x = const.$ through the center of the cyclone). This is what we find from the plot of the vertical velocity (figure 4.19b), and at these points we also observe strong uplifting of the isotherms while they stay at their initial position both in the center and outside of the cyclone (figure 4.20). Note that there is no significant upwelling exactly at the center since here (by construction of the windfield) the wind stress is zero. 2) It results in a mixed layer caused by the strong wind stress and parametrized by the KPP model. In this scheme the mixing depends (among other factors) on the wind stress at the surface, hence we expect the deepest mixed layer in the regions of strongest wind stress and fastest surface currents. Both is approximately true. The deepest mixed layer is indeed in the outskirts of the cyclone, however it is further outside than the maximum surface current speed (figure 4.24). Probably the mixed layer also depends on the divergence of the current (compare e.g. Run A_1) and indeed the mixed layer is largest where the divergence is negative (i.e. convergence takes place). Note that the mixed layer is also deepest in areas of negative windstress curl (figure 4.19a).

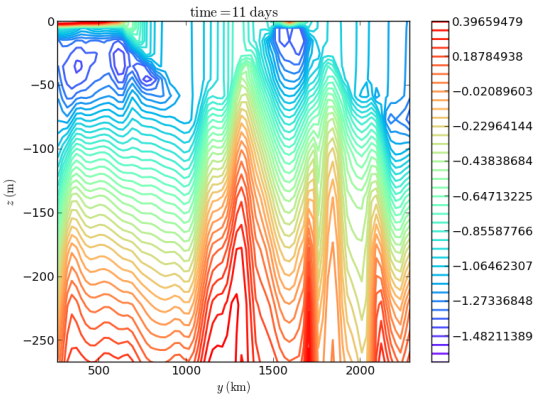

Figure 4.20: *Run C_3: θ at $x = 1500\,\mathrm{km}$, t = 3 days*

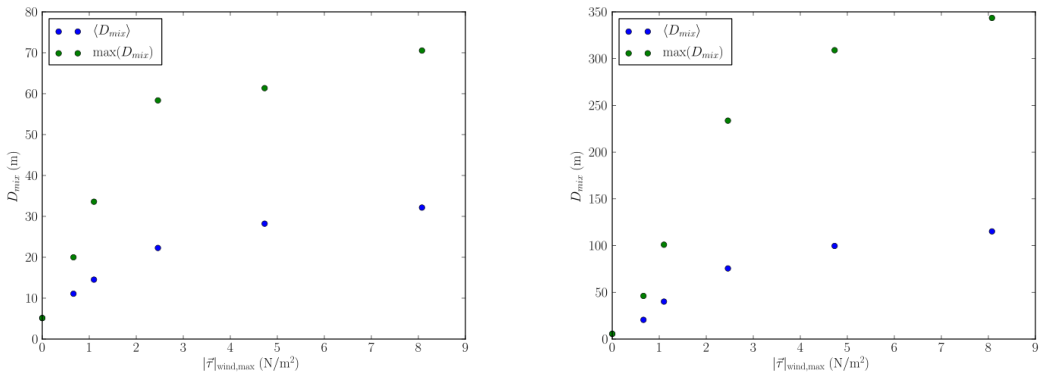

(a) *Runs C:* D_{mix} (m)*,* $t = 1$ *day* **(b)** *Runs C:* D_{mix} (m)*,* $t = 29$ *days*

Figure 4.21: *Runs C: Mixing depth as function of wind stress*

One finds, as expected, that the mixed layer depth deepens over time (figure 4.22). The increase especially in the average mixed layer is rather smooth and approximately linear. Note that even for one month of integration, the average mixed layer does not reach the thermocline (it might reach it in regions of higher than average mixing, combined with strong Ekman upwelling). The mixed layer depth also increases with wind stress (figure 4.21b). The relationship is clearly nonlinear, in particular one observes a leveling for large wind stresses. However, these stresses correspond already correspond to wind speeds $v_w > 40\,\mathrm{m\,s^{-1}}$. In the typical range of stresses ($\tau_w < 3\,\mathrm{N\,m^{-2}}$) the relationship is more linear. The dependence on the stress is about the same also for short integration times of only one day (figure 4.21a).

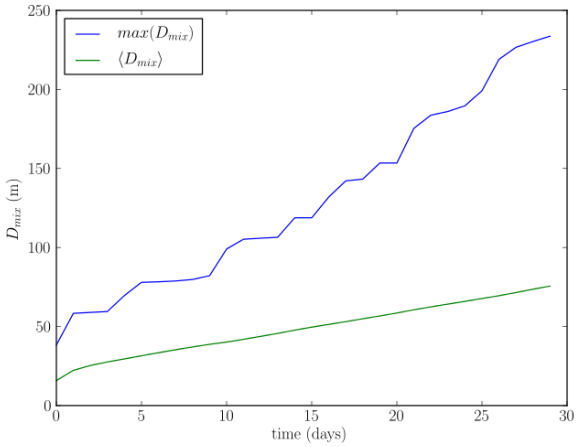

Figure 4.22: *Run C3:* D_{mix} (m) *as function of time*

These effects can be explained as follows: In areas of negative windstress curl the Ekman downwelling stretches the isopycnals close to the surface, hence already creating a more homogenous surface layer. This effect is reinforced by the convergence of the surface currents. The fast currents and relatively low stratification activate mixing through the KPP model which then causes an even deeper homogeneous layer, which is recognized as a mixed layer by the MITgcm diagnostic. Close to the center of the cyclone the effect is reversed: Ekman upwelling compresses the isopycnals close to the surface while divergence of the surface currents adds to the upwelling. Additionally, the wind speeds (and hence, surface current speeds) are lower. Hence the mixed layer generated by KPP mixing is much

shallower. In the center of the cyclone the wind is zero by construction of the wind forcing such that no mixing is initialized. The upwelling in neighboring regions also slightly shifts the isolines upwards here, but the warm water at the surface prevents a mixed layer to form.

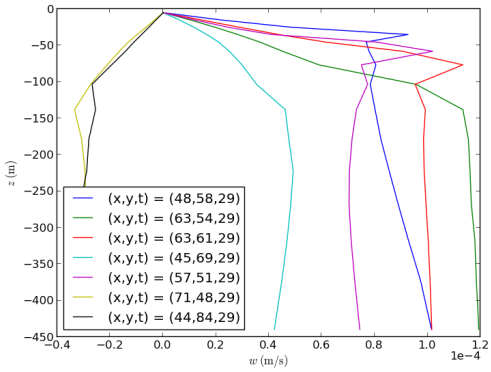

Figure 4.23: *Run C_3: Vertical velocity profile for various points, $t = 29$ days*

The Ekman depth is defined as the depth at which turbulent fluxes go to zero, and hence also the Ekman velocity w_E. The geostrophic velocity w_G however, is still present and constant if not acted against by other processes (section 2.8). Hence the boundary of the Ekman layer can be found by a plot of the vertical velocity over depth. In figure (4.23) we see that in this simulation the Ekman depth can be concluded to range between 50 m to 100 m.

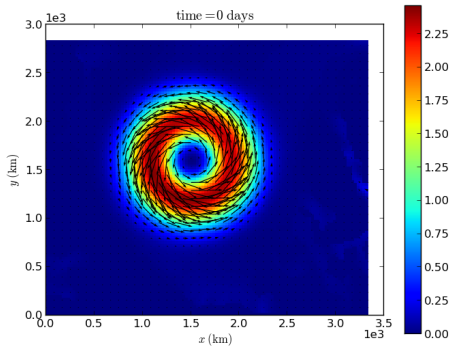

(a) τ_w $(\mathrm{N\,m^{-2}})$, $t = 0$ *days*

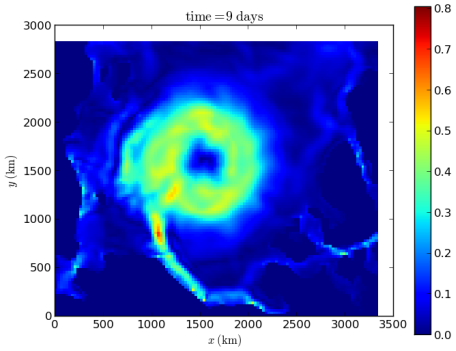

(b) $|\vec{v}|$ $(\mathrm{m\,s^{-1}})$, $t = 9$ *days*

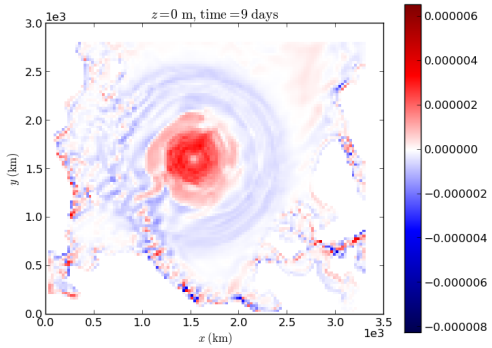

(c) $\nabla \cdot \vec{v}$ $(\mathrm{m\,s^{-2}})$, $t = 9$ *days*

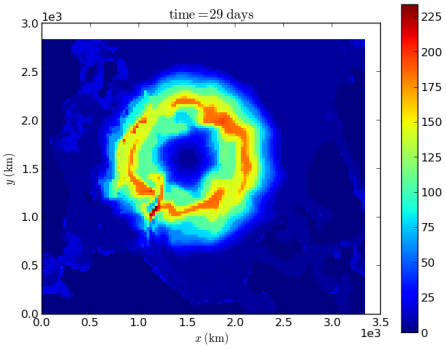

(d) D_{mix} (m), $t = 29$ *days*

Figure 4.24: *Run C_3: Mixing depth*

5 Conclusion

As mentioned in the introduction, the conducted simulations investigated whether it is possible to disturb the halocline and mix thermocline water masses to the surface by supplying (cyclonic) strong wind stress.

It has been shown that both LES and pan-Arctic simulations generate significant dynamics when forced with the described wind forcing. Ekman transport and upwelling, wind-driven currents and the establishment of a time- and forcing-dependent mixed layer were observed. The observations agree with expectations with regard to the different size and setup of the simulations. For instance, it was shown that the dynamics in the pan-Arctic simulations are much more dominated by rotational effects such as Ekman transport and upwelling than in the LES runs, as expected from the different domain sizes and resolutions, and hence e.g. different Ekman numbers. On the other hand, inertial and viscous effects were much more important in the LES runs. Note that the issue of unrealistic current patterns, including the convergence zones, as observed in series A was successfully resolved by applying a different wind forcing (series B).

The mixed layer depth was shown to increase as a function of the applied wind stress and time, showing a nonlinear dependence especially for large $\vec{\tau}_w$. This finding is consistent over all runs of both types of simulations that also agree in the approximate magnitudes. However, from the results it can be concluded that in neither simulation the mixed layer was deep enough to reach the temperature maximum at $\approx$ 300 to 400 m. This is even true for extremely strong forcing over one month of integration such as in run C_5.

The overall structure of the water column is only affected at the surface and in a limited region. Only for unrealistically long simulation times a change below $100 - 150$ m is observed (in those cases primarily via Ekman upwelling). Both halocline and thermocline stay largely intact and the sea surface is not warmed, but cooled via heat flux out of the ocean. After one day, the mixed layer reaches maximal depths of 55 m (series B) and 70 m (series C) for very strong winds ($41.89\,\mathrm{m\,s^{-1}}$ and $42.46\,\mathrm{m\,s^{-1}}$, respectively), while for more realistic speeds around $28\,\mathrm{m\,s^{-1}}$ the mixed layer reaches up to 45 m (series B) and 58 m (series C).

Moreover, the imposed cyclone does not lead to a warming of the sea surface. In the LES runs, upwelling did cause a temperature maximum in the center, however, it was both of low magnitude and contrasted with a cooling over most of the domain caused by the heat flux. In the pan-Arctic simulations, the sea surface temperature strongly increased due to the removal of the sea ice, but showed the smallest increase in areas under the influence of the cyclone (due to latent heat flux and distribution through mixing). Hence the cyclone can be concluded to actually have a cooling effect in this situation.

Hence the conclusion of this thesis is that even a very strong storm in a largely ice-free Arctic is unlikely to have drastic effects on the water column structure as we find it today.

In particular, it is unlikely to generate sufficient mixing to bring the warm water at ≈ 300 to 400 m to the surface.

While it was found that the mixed layer deepens with increasing wind, the question how the it depends on flow parameters such as current speed, divergence or turbulent viscosity has not yet been fully answers. Attempts were made in this regard, but the results are not yet very conclusive (figure 4.13). Further parameter studies could be conducted along these lines to shed more light on the issue.

Future studies could also investigate further how the water column structure might change in an ice-free Arctic ocean. Already the strong and fast temperature increase caused by the sea ice removal shows that such a situation would profoundly change the picture. Removing the sea ice will bring the sea surface into much closer contact with the atmosphere, and this could, on the long run, well have consequences for the water column and the dynamics in the Arctic ocean as a whole. Initially, as shown here, the increased sea surface temperature increases stratification by lowering the surface density. However, it is also possible that the increased temperature gives rise to even stronger storms which in turn could strongly affect the stability. Moreover, the sea ice also plays an important role for the salinity at the sea surface. Its removal could potentially increase the surface salinity, for instance through higher evaporation rates or through deeper mixing in an exposed upper ocean. Many other oceanic and atmospheric effects also play a role, such as the decrease in albedo or possible changes to the large-scale ocean and atmospheric circulation.

So, while this thesis suggest that the water column is very stable to perturbations, depending on which processes and feedbacks turn out to be the dominant ones over the long run, an ice-free Arctic Ocean could have either higher or lower stability. Future studies could investigate this further. An interesting example would be to run an ice-free scenario for a very long time to find out if just the removal is sufficient to significantly change the profile. Also, would this removal have other, long term or long range effects, such as a change in deepwater formation or ocean currents? Another possibility would be to do similar experiments as in this study with a coupled ocean-atmosphere model. This could well have quite different effects by strongly changing the albedo and enabling much stronger ocean-atmosphere interactions and feedbacks.

6 References

Adcroft, A. et al. (2013). *MITgcm User Manual*. MIT Department of EAPS.

Bentamy, A. et al. (2003). "Satellite estimates of wind speed and latent heat flux over the global oceans". In: *Journal of climate* 16.4, pp. 637–656.

Castro-Morales, K. et al. (2014). "Sensitivity of simulated Arctic sea ice to realistic ice thickness distributions and snow parameterizations". In: *Journal of Geophysical Research: Oceans* 119.1, pp. 559–571. ISSN: 2169-9291. DOI: 10.1002/2013JC009342. URL: http://dx.doi.org/10.1002/2013JC009342.

Daru, H. and C. Tenaud (2004). "High Order One-Step Monotonicity-Preserving Schemes for Unsteady Compressible Flow Calculations". In: *jcp* 193, pp. 563–594.

Griffies, S. and R. Hallberg (2000). "Biharmonic friction with a Smagorinsky-like viscosity for use in large-scale eddy-permitting ocean models". In: *Monthly Weather Review* 128.8, pp. 2935–2946.

Kara, A, P. Rochford, and H. Hurlburt (2000). "An optimal definition for ocean mixed layer depth". In: *Journal of Geophysical Research: Oceans* 105.C7, pp. 16803–16821. ISSN: 2156-2202. DOI: 10.1029/2000JC900072. URL: http://dx.doi.org/10.1029/2000JC900072.

Large, W., J. McWilliams, and S. Doney (1994). "Oceanic vertical mixing: A review and a model with a nonlocal boundary layer parameterization". In: *Reviews of Geophysics* 32.4, pp. 363–403. ISSN: 1944-9208. DOI: 10.1029/94RG01872. URL: http://dx.doi.org/10.1029/94RG01872.

Large, W. and S. Yeager (2009). "The global climatology of an interannually varying airsea flux data set". In: *Climate Dynamics* 33.2-3, pp. 341–364. ISSN: 0930-7575. DOI: 10.1007/s00382-008-0441-3. URL: http://dx.doi.org/10.1007/s00382-008-0441-3.

Manneville, P. (2004). *Instabilities, chaos and turbulence: An introduction to nonlinear dynamics and complex systems*. Vol. 1. Imperial College Pr.

Marshall, J. et al. (1997a). "A finite-volume, incompressible Navier Stokes model for studies of the ocean on parallel computers". In: *Journal of Geophysical Research: Oceans (1978–2012)* 102.C3, pp. 5753–5766.

Miles, J. (1961). "On the stability of heterogeneous shear flows". In: *Journal of Fluid Mechanics* 10.04, pp. 496–508.

Pedlosky, J. (1987). *Geophysical fluid dynamics*. 2nd ed. Vol. 1. Springer-Verlag, New York and Berlin.

Peterson, B. et al. (2002). "Increasing River Discharge to the Arctic Ocean". In: *Science* 298.5601, pp. 2171–2173. DOI: 10.1126/science.1077445. eprint: http://www.sciencemag.org/content/298/5601/2171.full.pdf. URL: http://www.sciencemag.org/content/298/5601/2171.abstract.

Polton, J. and S. Belcher (2007). "Langmuir turbulence and deeply penetrating jets in an unstratified mixed layer". In: *Journal of Geophysical Research: Oceans* 112.C9, n/a–

n/a. ISSN: 2156-2202. DOI: 10.1029/2007JC004205. URL: http://dx.doi.org/10.1029/2007JC004205.

Pond, S. and G. Pickard (1983). *Introductory dynamical oceanography*. 2nd ed. Butterworth Heinemann.

Proshutinsky, A. and M. Johnson (1997). "Two circulation regimes of the wind-driven Arctic Ocean". In: *Journal of Geophysical Research: Oceans* 102.C6, pp. 12493–12514. ISSN: 2156-2202. DOI: 10.1029/97JC00738. URL: http://dx.doi.org/10.1029/97JC00738.

Rudels, B., L. Anderson, and E. Jones (1996). "Formation and evolution of the surface mixed layer and halocline of the Arctic Ocean". In: *Journal of Geophysical Research: Oceans* 101.C4, pp. 8807–8821. ISSN: 2156-2202. DOI: 10.1029/96JC00143. URL: http://dx.doi.org/10.1029/96JC00143.

Simmonds, I. and I. Rudeva (2012). "The great Arctic cyclone of August 2012". In: *Geophysical research letters* 39.23.

Smagorinksy, J. (1963). "General circulation experiments with the primitive equations: I. The basic experiment". In: *Monthly weather review* 91.3, pp. 99 –164.

Smagorinsky, J. (1993). "Some historical remarks on the use of nonlinear viscosities". In: *Large eddy simulation of complex engineering and geophysical flows*. Ed. by Boris Galperin and Steven A Orszag. Cambridge University Press.

Smyth, W. and J. Moum (2012). "Ocean mixing by Kelvin-Helmholtz instability". In: *Oceanography* 25.2, pp. 140 –149. DOI: 10.5670/oceanog.2012.49.

Steele, M. and T. Boyd (1998). "Retreat of the cold halocline layer in the Arctic Ocean". In: *Journal of Geophysical Research: Oceans (1978–2012)* 103.C5, pp. 10419–10435.

Steele, M., R. Morley, and W. Ermold (2001). "PHC 3.0, updated from: PHC: A global ocean hydrography with a high quality Arctic Ocean". In: *J. Climate* 14.8, pp. 2079–2087.

Stewart, R. (2008). *Introduction to Physical Oceanography*. Texas A & M University.

Sverdrup, H., M. Johnson, and R. Fleming (1942). *The oceans: their physics, chemistry, and general biology*. Vol. 7. Prentice-Hall New York.

Vavrus, S. et al. (2012). "Twenty-First-Century Arctic Climate Change in CCSM4". In: *Journal of Climate* 25, pp. 2696–2710.

Wang, M. and J. Overland (2009). "A sea ice free summer Arctic within 30 years?" In: *Geophysical Research Letters* 36.7, p. L07502.

Zhang, J. et al. (2013). "The impact of an intense summer cyclone on 2012 Arctic sea ice retreat". In: *Geophysical Research Letters* 40, pp. 720–726.

A Appendix

A.1 LES

A.1.1 2D Runs

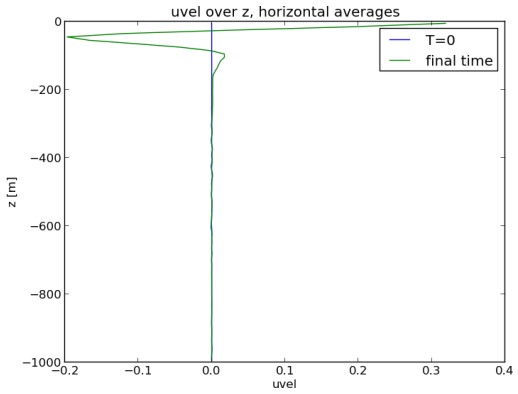

Figure A.1: *Run 4: Zonal Velocity, horizontally averaged, after 24 hours*

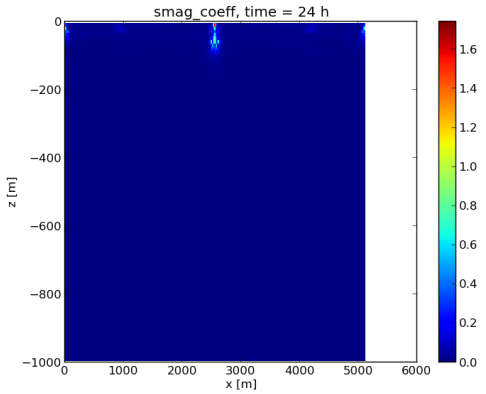

Figure A.2: *Run 1: Smagorinsky viscosity after 24 hours*

A.1.2 Series A

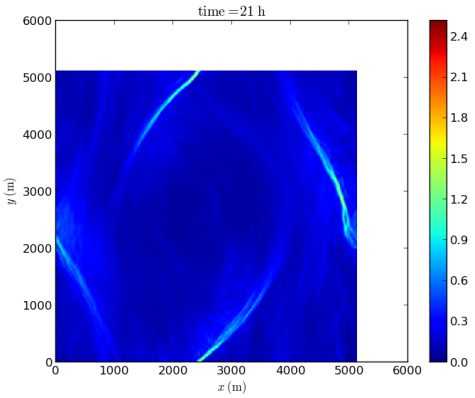

Figure A.3: *Run A_1: $A_{h,Smag}$ in $\mathrm{m^2\,s^{-1}}$, $t = 52$ h*

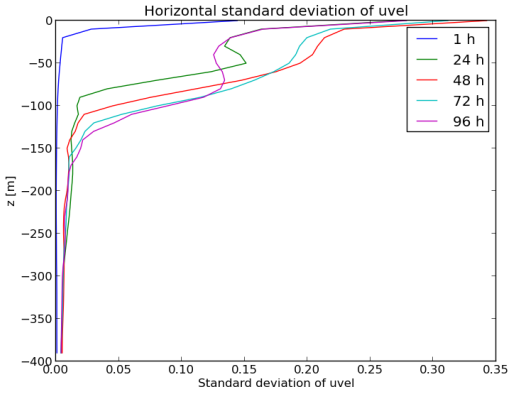

Figure A.4: *Run A_1: Horizontal standard deviation of zonal velocity*

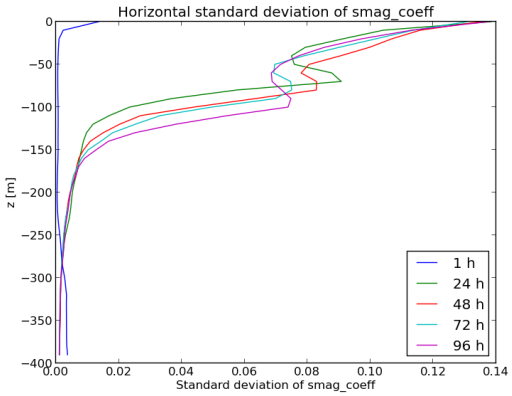

Figure A.5: *Run A_1: Horizontal standard deviation of Smagorinsky viscosity*

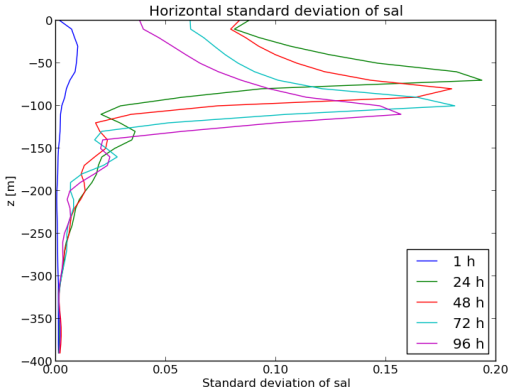

Figure A.6: *Run A_1: Horizontal standard deviation of Salinity*

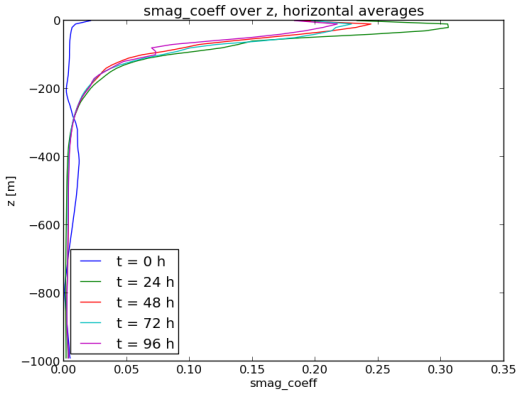

Figure A.7: *Run A_2: Smagorinsky Viscosity, horizontally averaged*

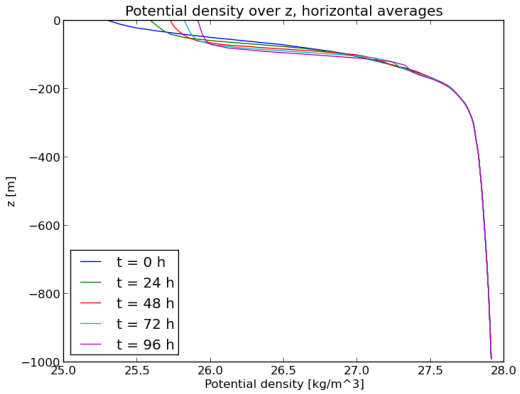

Figure A.8: *Run A_2: Potential Density, horizontally averaged*

A.1.3 Series B

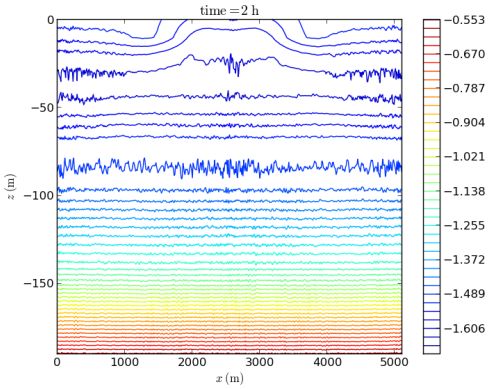

Figure A.9: *Run B_3: Temperature* °C *at* $y = 2560\,\mathrm{m}$

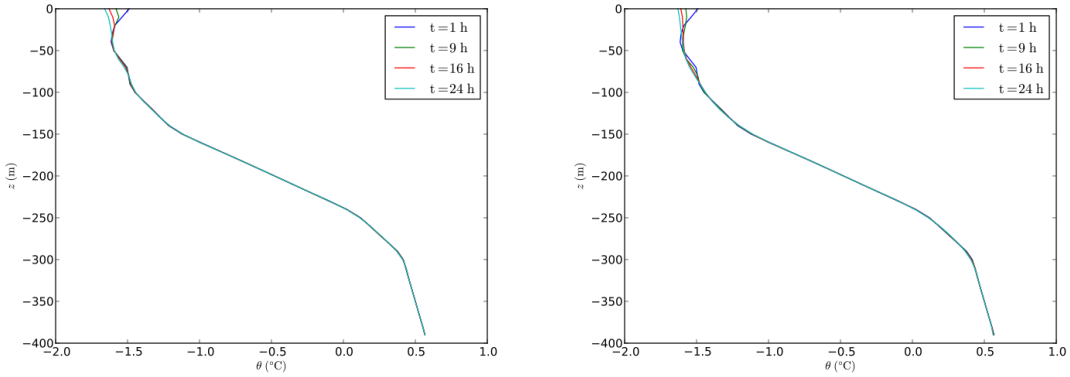

(a) *Run B_3* **(b)** *Run B_6*

Figure A.10: *Horizontal average of θ in* °C

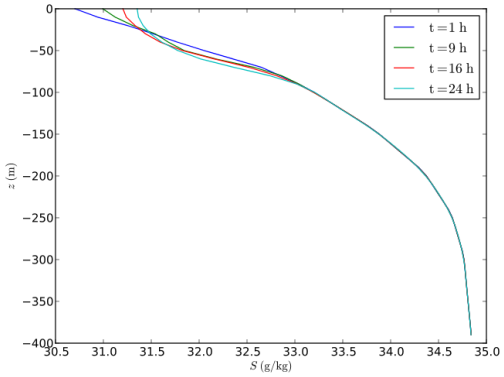

Figure A.11: *Run B_6: Horizontal average of S in* $\mathrm{g\,kg^{-1}}$

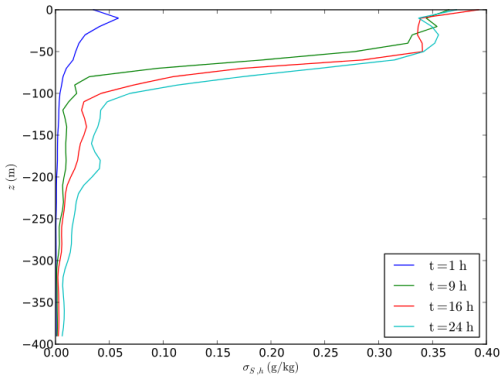

Figure A.12: *Run B_6: Standard deviation of salinity σ_S in* $\mathrm{g\,kg^{-1}}$

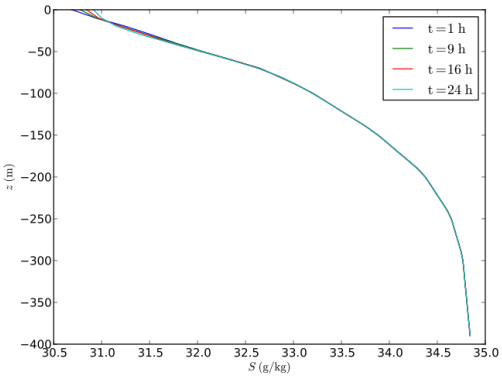

(a) *Run B_1: S in* $\mathrm{g\,kg^{-1}}$

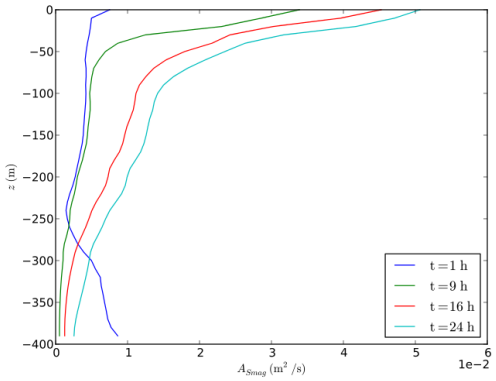

(b) *Run B_1: $A_{h,smag}$ in* $\mathrm{m^2\,s^{-1}}$

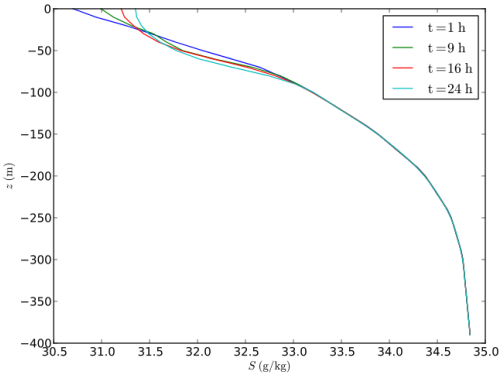

(c) *Run B_6: S in* $\mathrm{g\,kg^{-1}}$

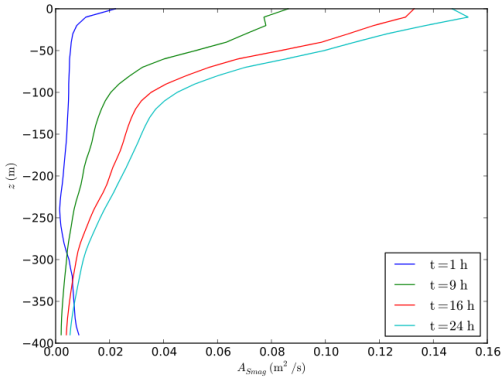

(d) *Run B_6: $A_{h,smag}$ in* $\mathrm{m^2\,s^{-1}}$

Figure A.13: *Horizontal averages for runs B_1 and B_6*

A.2 Pan-Arctic Simulations (Series C)

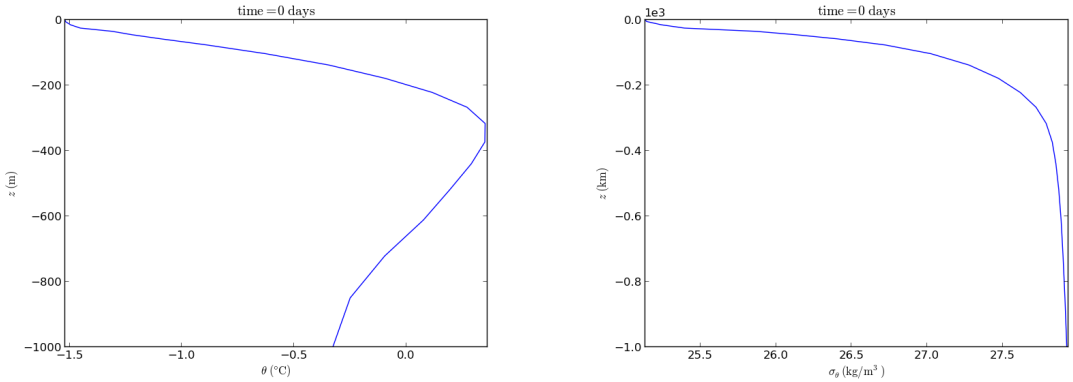

(a) θ *in* °C, t = *0 days* **(b)** σ_θ *in* $\mathrm{kg\,m^{-3}}$, t = *0 days*

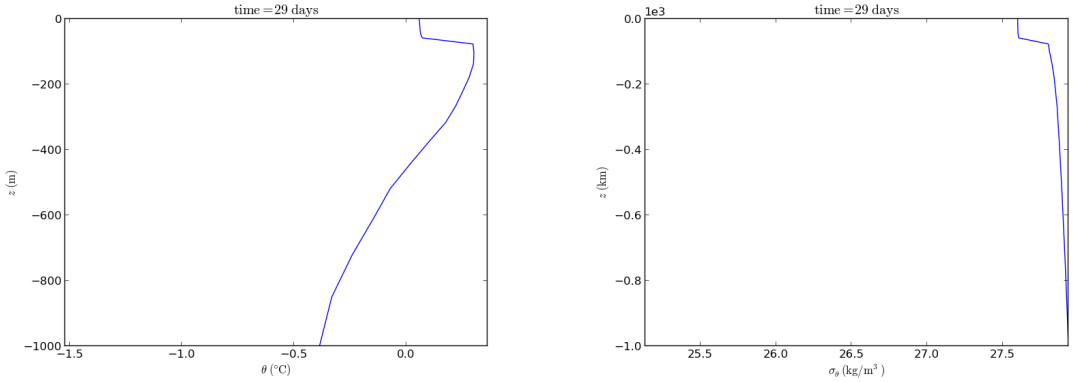

(c) θ *in* °C, t = *29 days* **(d)** σ_θ *in* $\mathrm{kg\,m^{-3}}$, t = *0 days*

Figure A.14: *Run C_5: θ- and σ_θ-profile at (x,y) = (54,41)*

B Acknowledgments

I would like to thank the Alfred-Wegener Institute (AWI) for the opportunity to write this thesis, in particular Prof. Dr. Thomas Jung for suggesting the topic to me and supporting me in pursuing it, as well as all members of the Climate Dynamics section for welcoming me into their group and for many interesting conversations. Many thanks go to my supervisor Dr. Martin Losch, for his constant support, suggestions and help in discussing the findings. Thanks go as well to Dr. Kathrin Riemann-Campe for introducing me to computational oceanography more than one year ago and for support regarding the Pan-Arctic simulations. And, of course, Prof. Dr. Joachim Vogt earns many thanks for his advice, support on campus and constant suggestions about further ideas that could be explored.

C Declaration

With my signature, I certify that this thesis has been written by me using only the indicated resources and materials. Where I have presented data and results, the data and results are complete, genuine, and have been obtained by me unless otherwise acknowledged; where my results derive from computer programs, these computer programs have been written by me unless otherwise acknowledged. I further confirm that this thesis has not been submitted, either in part or as a whole, for any other academic degree at this or another institution.

Place, Date	Signature